

LJMU Research Online

Pearson, J, Subrayan, B, Sand, DJ, Andrews, JE, Beasor, ER, Bostroem, KA, Dong 董, Y 一泽, Hoang, E, Hosseinzadeh, G, Hsu, B, Jacobson-Galán, W, Janzen, D, Jencson, J, Jha, SW, Kilpatrick, CD, Kwok, LA, Liu, C, Lundquist, MJ, Mehta, D, Miller, AA, Ravi, AP, Rehemtulla, N, Meza Retamal, N, Shrestha, M, Smith, N, Valenti, S and Whitler, L

Mid-infrared Dust Evolution and Late-time Circumstellar Medium Interaction in SN 2017eaw

https://researchonline.ljmu.ac.uk/id/eprint/27566/

Article

Citation (please note it is advisable to refer to the publisher's version if you intend to cite from this work)

Pearson, J ORCID logoORCID: https://orcid.org/0000-0002-0744-0047, Subrayan, B ORCID logoORCID: https://orcid.org/0000-0001-8073-8731, Sand, DJ ORCID logoORCID: https://orcid.org/0000-0003-4102-380X, Andrews. JE ORCID logoORCID: https://orcid.org/0000-0003-0123-0062.

LJMU has developed LJMU Research Online for users to access the research output of the University more effectively. Copyright © and Moral Rights for the papers on this site are retained by the individual authors and/or other copyright owners. Users may download and/or print one copy of any article(s) in LJMU Research Online to facilitate their private study or for non-commercial research. You may not engage in further distribution of the material or use it for any profit-making activities or any commercial gain.

The version presented here may differ from the published version or from the version of the record. Please see the repository URL above for details on accessing the published version and note that access may require a subscription.

For more information please contact researchonline@ljmu.ac.uk



OPEN ACCESS



Mid-infrared Dust Evolution and Late-time Circumstellar Medium Interaction in SN 2017eaw

Lindsey A. Kwok¹², Chang Liu^{11,12}, M. J. Lundquist¹³, Darshana Mehta⁵, Adam A. Miller^{11,12,14}, Aravind P. Ravi⁵, Nabeel Rehemtulla 11,12,14, Nicolás Meza Retamal 6, Manisha Shrestha 6, Nathan Smith 6, Stefano Valenti 6, and Lily Whitler 100 ¹ Steward Observatory, University of Arizona, 933 North Cherry Avenue, Tucson, AZ 85721-0065, USA; jenivevepearson@arizona.edu Gemini Observatory, 670 North A'ohoku Place, Hilo, HI 96720-2700, USA ³ Astrophysics Research Institute, Liverpool John Moores University, 146 Brownlow Hill, Liverpool, L3 5RF, UK Center for Astrophysics | Harvard & Smithsonian, 60 Garden Street, Cambridge, MA 02138-1516, USA ⁵ Department of Physics and Astronomy, University of California, Davis, 1 Shields Avenue, Davis, CA 95616-5270, USA ⁶ Department of Astronomy & Astrophysics, University of California, San Diego, 9500 Gilman Drive, MC 0424, La Jolla, CA 92093-0424, USA Department of Astronomy and Astrophysics, California Institute of Technology, Pasadena, CA 91125, USA ⁸ Department of Physics & Engineering Physics, University of Saskatchewan, 116 Science Place, Saskatoon, SK S7N 5E2, Canada ⁹ IPAC, Mail Code 100-22, Caltech, 1200 East California Boulevard, Pasadena, CA 91125, USA Department of Physics and Astronomy, Rutgers, the State University of New Jersey, 136 Frelinghuysen Road, Piscataway, NJ 08854-8019, USA
Department of Physics and Astronomy, Northwestern University, 2145 Sheridan Road, Evanston, IL 60208, USA ¹² Center for Interdisciplinary Exploration and Research in Astrophysics (CIERA), 1800 Sherman Avenue, Evanston, IL 60201, USA W. M. Keck Observatory, 65-1120 Māmalahoa Highway, Kamuela, HI 96743-8431, USA ¹⁴ NSF-Simons AI Institute for the Sky (SkAI), 172 East Chestnut Street, Chicago, IL 60611, USA Received 2025 June 30; revised 2025 August 5; accepted 2025 August 19; published 2025 November 5

Abstract

We present JWST/Mid-Infrared Instrument (MIRI) and complementary ground-based near-infrared observations of the Type II SN 2017eaw taken 6 yr postexplosion. SN 2017eaw is still detected out to 25 μ m and there is minimal evolution in the mid-infrared spectral energy distribution (SED) between the newly acquired JWST/MIRI observations and those taken a year earlier. Modeling of the mid-infrared SED reveals a cool ~160 K dust component of $5.5 \times 10^{-4} \, M_{\odot}$ and a hot ~1700 K component of $5.4 \times 10^{-8} \, M_{\odot}$, both composed of silicate dust. Notably, there is no evidence of temperature or mass evolution in the cool dust component in the year between JWST observations. We also present new and archival HST and ground-based ultraviolet (UV) and optical observations which reveal reduced but continued circumstellar medium (CSM)–ejecta interaction at >2000 days postexplosion. The UV and mid-infrared emission show similar decline rates, suggesting both probe the interface between the ejecta and CSM. Given the continued existence of boxy $H\alpha$ emission in the nebular spectra, the low inferred optical depth of the dust, and the lack of temperature and mass evolution, we suggest that the cool dust component in SN 2017eaw may be primarily due to pre-existing dust rather than newly formed dust in the ejecta or cold dense shell.

Unified Astronomy Thesaurus concepts: Circumstellar matter (241); Core-collapse supernovae (304); Dust formation (2269); Massive stars (732); Supernovae (1668); Type II supernovae (1731)

Materials only available in the online version of record: data behind figure, figure set, machine-readable tables

1. Introduction

Observations of high-redshift galaxies have revealed significant amounts of dust in the early Universe (D. P. Marrone et al. 2018; T. Hashimoto et al. 2019; J. Witstok et al. 2023; V. Markov et al. 2024; A. Nanni et al. 2025). The majority of this dust is likely associated with core-collapse supernovae (CCSNe; H. L. Morgan & M. G. Edmunds 2003; R. Maiolino et al. 2004; C. Gall et al. 2011; R. Schneider & R. Maiolino 2024). Models of high-redshift supernovae (SNe) and star formation rates indicate that SNe would need to

Original content from this work may be used under the terms of the Creative Commons Attribution 4.0 licence. Any further distribution of this work must maintain attribution to the author(s) and the title of the work, journal citation and DOI.

produce between 0.1 and 1 M_{\odot} of dust per SN (P. Todini & A. Ferrara 2001; A. Sarangi et al. 2018; R. Schneider & R. Maiolino 2024) and observations of nearby SN remnants have revealed dust masses within this range (L. Dunne et al. 2003; H. L. Morgan et al. 2003; J. Rho et al. 2008; I. De Looze et al. 2017; J. Chastenet et al. 2022; F. D. Priestley et al. 2022). However, the vast majority of near-infrared (NIR) and midinfrared studies of nearby SNe undertaken prior to JWST have revealed significantly lower dust masses ($\lesssim 10^{-2} M_{\odot}$; C. Gall et al. 2011; T. Szalai & J. Vinkó 2013; S. Tinyanont et al. 2016; T. Szalai et al. 2019b). These previous studies therefore suggest that infrared observations of CCSNe in the decades after explosion may be missing a significant portion of the dust.

Dust formation in SNe likely occurs in the expanding ejecta interior to the reverse shock and/or in a cold dense shell between the forward and reverse shock created by the interaction between the forward shock and surrounding dense circumstellar material (CSM; e.g., M. Pozzo et al. 2004; S. Mattila et al. 2008; N. Smith et al. 2008, 2009). In the decades to centuries following the SN,

¹⁵ LSST-DA Catalyst Fellow.

¹⁶ NASA Hubble Fellow.

some of the dust in the interior ejecta will be destroyed by interaction with the reverse shock; however, some percentage is expected to survive this interaction and facilitate further dust formation (S. Bianchi & R. Schneider 2007; T. Nozawa et al. 2007; D. W. Silvia et al. 2010). There are some indications that the majority of newly formed dust in the first years postexplosion in noninteracting hydrogen-rich CCSNe (e.g., type IIP/L SNe) is interior and optically thick, and thus only visible in the spectral line profiles and not in infrared images. Studies modeling the optical nebular spectra of noninteracting H-rich SNe recover higher dust masses than indicated by infrared photometry alone (M. Niculescu-Duvaz et al. 2022; S. Zsíros et al. 2024). Furthermore, the significant dust mass in SN 1987A is only observable in the far-infrared and submillimeter (P. Bouchet et al. 2006; M. Matsuura et al. 2011, 2015; R. Indebetouw et al. 2014; P. Cigan et al. 2019). Thus, even in the case where the dust is optically thin, any newly formed dust may be too cold to detect in the NIR/mid-infrared.

Measuring dust formation in SNe is further complicated by the presence of pre-existing dust in the CSM. Dust directly around the progenitor is destroyed immediately following the explosion but pre-SN dust can survive at further distances. This pre-existing dust can be formed within the CSM in the stellar winds and/or binary interactions of massive stars. This dust is warmed by the SN explosion and subsequent ejecta—CSM interaction, becoming visible in the infrared (e.g., B. E. K. Sugerman 2003; R. Kotak et al. 2009; O. D. Fox et al. 2010). Dust in nearby SNe is likely both pre-existing in the CSM and created in the ejecta. However, only a handful of SNe have the multiepoch, multiwavelength measurements that are crucial to disentangle the origin of the dust, and therefore constrain the timeline of CCSNe dust formation.

The launch of JWST has ushered in a new era of SN dust studies. JWST's sensitivity, resolution, and wavelength coverage has allowed for observations that probe both hot and cool dust around the SNe in the years following collapse. In concert with multiwavelength ground- and space-based observations, numerous studies have utilized JWST data to constrain the dust formation around some of the nearest SNe (R. G. Arendt et al. 2023; G. Hosseinzadeh et al. 2023b; O. C. Jones et al. 2023; M. Shahbandeh et al. 2023, 2024, 2025; P. Bouchet et al. 2024; S. Gomez et al. 2024; M. Matsuura et al. 2024; S. Zsíros et al. 2024; G. C. Clayton et al. 2025; A. Sarangi et al. 2025; T. Szalai et al. 2025; S. Tinyanont et al. 2025). This growing data set is vital to understanding the onset of dust production in CCSNe and its impact on the evolution of the early Universe.

In this paper, we present an analysis of newly acquired and archival multiwavelength observations of SN 2017eaw, the first SN with multiepoch late-time mid-infrared JWST observations. We review the observational data and reduction techniques in Section 2. In Section 3, we analyze the ultraviolet (UV) and infrared photometry, determine the extent of mid-infrared evolution, and model the dust SED. We discuss the possible origin of SN 2017eaw's dust in Section 4 and conclude in Section 5.

2. Observations

SN 2017eaw was discovered on 2017 May 14 in NGC 6946, a nearby galaxy ($D \approx 7.12$ Mpc according to the latest TRBG distance¹⁷) with a high SN rate (see Figure 1). SN 2017eaw

has extensive multiwavelength observations, both pre- and postexplosion (explosion on 57885.2 MJD S. D. Van Dyk et al. 2019), and has been the subject of numerous studies (e.g., C. D. Kilpatrick & R. J. Foley 2018; J. Rho et al. 2018; D. Y. Tsvetkov et al. 2018; R. J. Buta & W. C. Keel 2019; L. Rui et al. 2019; T. Szalai et al. 2019a; S. Tinyanont et al. 2019; S. D. Van Dyk et al. 2019; K. A. Bostroem et al. 2023; M. Shahbandeh et al. 2023; K. E. Weil et al. 2020).

There is significant evidence of ejecta–CSM interaction in SN 2017eaw. Pre-explosion Spitzer Space Telescope (hereafter Spitzer) images show the progenitor star was surrounded by a dusty shell at \sim 4000 R_{\odot} (C. D. Kilpatrick & R. J. Foley 2018). Early time detections of SN 2017eaw in the X-ray, UV, and radio indicate moderate interaction between the SN shock and the CSM (T. Szalai et al. 2019a). Furthermore, the optical light curve of SN 2017eaw exhibits a bump peaking around a week postexplosion that further suggests early time CSM interaction (T. Szalai et al. 2019a). Years after explosion, there remain signs of ongoing ejecta-CSM interaction. Hubble Space Telescope (HST) near-UV imaging reveals the SN is still UV bright (as shown in Figure 1; S. D. Van Dyk et al. 2023), light curves of the SN out to 1500 days indicate a shallower decline than expected for pure radioactive decay (M. Rizzo Smith et al. 2023), and late-time (>900 days postexplosion) optical spectra exhibit boxy line profiles indicating that the ejecta is continuing to collide with the surrounding material (K. E. Weil et al. 2020; M. Shahbandeh et al. 2023). Given the continued detection of CSM interaction, it is likely that some pre-existing dust surrounds SN 2017eaw.

In addition to the presence of dust in the CSM, there are several observational indicators that SN 2017eaw is producing dust in its ejecta. CO was detected in the NIR spectra roughly one year postexplosion, demonstrating that the temperature of the ejecta has cooled enough for dust formation (J. Rho et al. 2018; S. Tinyanont et al. 2019). Furthermore, nebular spectra of SN 2017eaw reveal blueshifted and asymmetric line profiles indicative of dust in the ejecta (J. Rho et al. 2018; K. E. Weil et al. 2020; M. Shahbandeh et al. 2023). The likely presence of both pre-existing and newly formed dust in SN 2017eaw makes it an ideal test case for understanding when newly formed dust begins to dominate the infrared dust spectral energy distribution (SED).

Postexplosion infrared observations of SN 2017eaw were executed by both Spitzer and JWST. Ground-based NIR and Spitzer observations (3.6 and 4.5 μ m) at 200 and 500 days postexplosion and JWST mid-infrared observations at ~2000 days reveal a population of observed silicate dust that has increased in mass over the years (from ~1 × 10⁻⁴ to 5.5 × 10⁻⁴ M_{\odot} S. Tinyanont et al. 2019; M. Shahbandeh et al. 2023). However, given the proximity of the Spitzer observations to explosion and the limited wavelength coverage, it is difficult to determine if the Spitzer and JWST dust populations are related.

We present the second epoch of mid-infrared JWST imaging of SN 2017eaw, taken one year after the first, and compare it directly to the previously published epoch in order to determine the nature and origin of the dust. To further understand the dust evolution of SN 2017eaw, we also collect and analyze additional new and archival data, including optical and near-UV HST observations and ground-based optical and infrared imaging and spectroscopy.

¹⁷ https://edd.ifa.hawaii.edu/get_cmd.php?pgc=65001, this distance is also used in M. Shahbandeh et al. (2023).

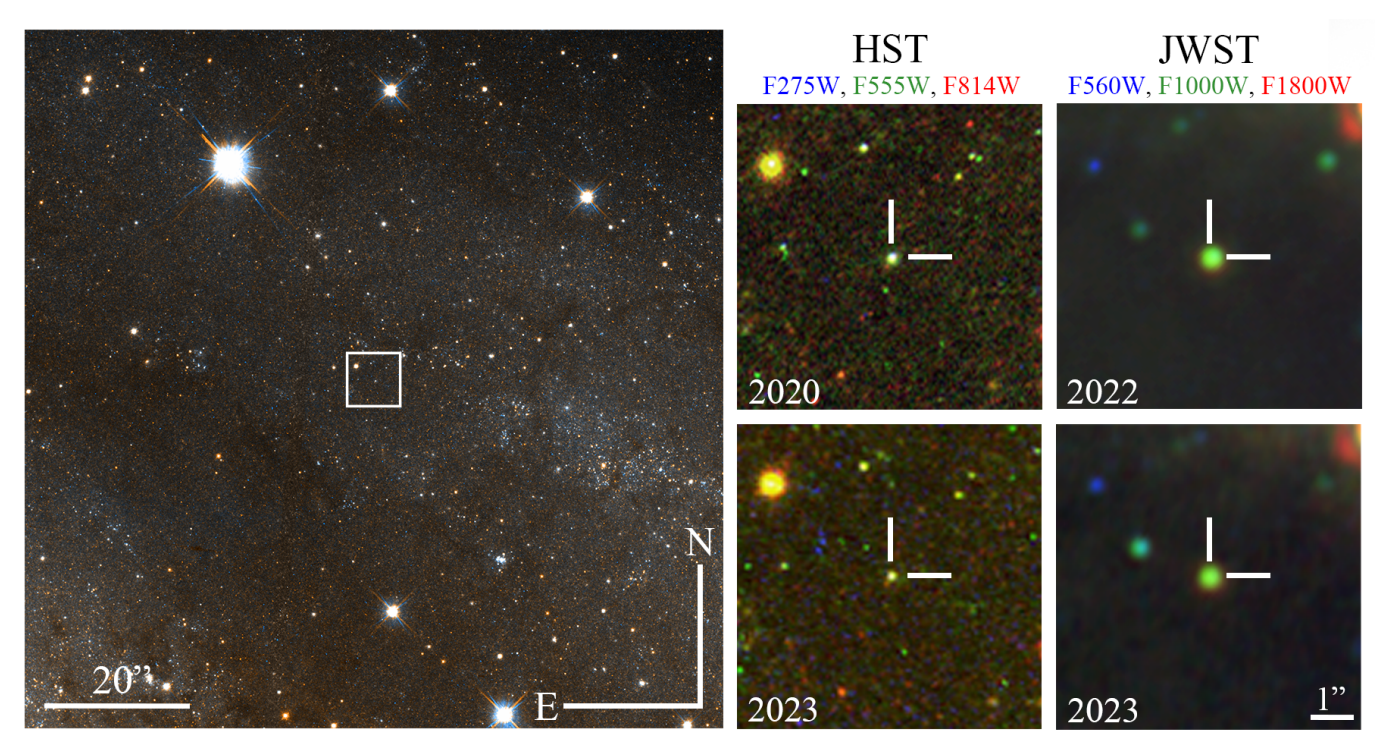


Figure 1. Red, green, and blue false color images of SN 2017eaw using archival and recently acquired Hubble Space Telescope (F275W, F555W, and F814W) and JWST (F560W, F1000W, and F1800W) observations. The larger finder on the left was made with the F555W (60299 MJD) and F814W (59924 MJD) Hubble Space Telescope images taken in 2023.

2.1. JWST/MIRI

Initial JWST Mid-Infrared Instrument (MIRI; P. Bouchet et al. 2015; G. H. Rieke et al. 2015; G. S. Wright et al. 2023) imaging of SN 2017eaw taken using the F560W, F1000W, F1130W, F1280W, F1500W, F1800W, F2100W, and F2550W filters was obtained in 2022 September (1957.7 days postexplosion) as part of the Cycle 1 General Observers (GO) 2666 Program (O. D. Fox et al. 2021). Photometry and analysis of this epoch was previously published in M. Shahbandeh et al. (2023).

Further JWST/MIRI observations of SN 2017eaw were also obtained on 2023 September 26 (2328.2 days postexplosion) as part of the Cycle 2 GO 3295 Program (D. J. Sand et al. 2023). These observations were taken with the complete set of MIRI filters (F560W, F770W, F1000W, F1130W, F1280W, F1500W, F1800W, F2100W, and F2550W), using the FULL array with a FASTR1 readout pattern, a four-point dither pattern, and an exposure time of 111 s for all filters.

Given that one focus of this work is on the flux evolution between the Cycle 1 and 2 observations, we opt to reanalyze photometry of the Cycle 1 data so that the methodology remains consistent between epochs. In this work, both the Cycle 1 and Cycle 2 JWST observations of SN 2017eaw were processed with the JWST Calibration Pipeline version 1.15.1, with the Calibration Reference Data System version 11.17.25 (H. Bushouse et al. 2025).

We attempt aperture photometry on the Cycle 1 and 2 images using several different methods, outlined in Appendix A. However, M. Shahbandeh et al. (2023) report point-spread function (PSF) photometry for SN 2017eaw, and we find that our aperture photometry methods result in flux values for the Cycle 1 observations which are 10%–40% higher than those reported in M. Shahbandeh et al. (2023). For

consistency with the published photometry, we instead report PSF photometry done using space_phot¹⁸ (J. Pierel 2024; J. D. R. Pierel et al. 2024). We note that this choice does not significantly impact the conclusions of this work since they are based primarily on the difference between the JWST/MIRI epochs and not the absolute flux calibration. PSF photometry with space phot is done on the stage 2 products for all filters except F2550W. This involves fitting the SN's PSF in each of the four individual Level 2 CAL files using WebbPSF (M. D. Perrin et al. 2012, 2014, version 1.2.1) models. Given the low signal-to-noise detection of SN 2017eaw in F2550W, we opt to do PSF photometry on the Level 3 stacked images for this filter. The space_phot routine for Level 3 photometry uses temporally and spatially dependent Level 2 PSF models from WebbPSF, and drizzles them together to create a Level 3 PSF model. While the MIRI PSF models have been significantly updated since the publication of M. Shahbandeh et al. (2023), we find our Cycle 1 PSF photometry is mostly consistent with the previously reported values (see Appendix A for more information). We report the flux values from space_phot for both the Cycle 1 and Cycle 2 observations in Table 1.

2.2. HST Optical and UV

Several HST observations of SN 2017eaw have been taken since explosion (see Table 2). S. D. Van Dyk et al. (2023) reported HST photometry of SN 2017eaw from late 2020 and early 2022 as part of their study of the progenitor. Since then, observations in ACS/WFC F555W and F814W (PI: C. Kilpatrick, ID: 17070) and WFC3/UVIS F275W and F555W

⁸ space_phot version 0.2.5 https://space-phot.readthedocs.io.

Table 1
JWST/MIRI Cycle 1 and 2 Observations of SN 2017eaw

	Cycle 1				Cycle 2			
Filter	MJD	Phase ^a (days)	Flux Density (μJy)	AB Mag	MJD	Phase (days)	Flux Density (μJy)	AB Mag
F560W	59842.885	1957.7	5.99 ± 0.14	21.957 ± 0.025	60213.391	2328.2	3.45 ± 0.12	22.555 ± 0.038
F770W	•••				60213.394	2328.2	7.64 ± 0.17	21.692 ± 0.024
F1000W	59842.896	1957.7	54.79 ± 0.15	19.553 ± 0.003	60213.405	2328.2	41.53 ± 0.45	19.854 ± 0.012
F1130W	59842.906	1957.7	53.63 ± 0.62	19.576 ± 0.012	60213.409	2328.2	38.70 ± 1.27	19.931 ± 0.035
F1280W	59842.913	1957.7	42.76 ± 0.66	19.822 ± 0.017	60213.417	2328.2	34.58 ± 1.02	20.053 ± 0.032
F1500W	59842.919	1957.7	60.42 ± 1.14	19.447 ± 0.020	60213.422	2328.2	47.30 ± 1.97	19.713 ± 0.044
F1800W	59842.927	1957.7	101.49 ± 3.48	18.884 ± 0.037	60213.428	2328.2	108.20 ± 6.20	18.814 ± 0.060
F2100W	59842.935	1957.7	112.15 ± 6.69	18.776 ± 0.063	60213.436	2328.2	107.88 ± 14.86	18.818 ± 0.140
F2550W	59842.941	1957.7	106.67 ± 10.24	18.830 ± 0.100	60213.439	2328.2	69.71 ± 20.34	19.292 ± 0.278

Note.

(This table is available in machine-readable form in the online article.)

(PI: W. Jacobson-Galan, ID: 17506) in late 2022 and late 2023, respectively, have been completed.

We use DOLPHOT (A. E. Dolphin 2000; A. Dolphin 2016) to obtain PSF photometry of SN 2017eaw in all HST images. We use the calibrated and charge-transfer-efficiency corrected flc and the corresponding drizzled drc frames from the Mikulski Archive for Space Telescopes as inputs for DOLPHOT. Each epoch and filter combination was run through DOLPHOT separately and the flc frames were aligned to the associated drc image. We use the same DOLPHOT parameter settings as were used for the HST PHAT survey (J. J. Dalcanton et al. 2012; B. F. Williams et al. 2014). DOLPHOT detected a "good" star ("object type" = 1) at the location of SN 2017eaw in all filters and epochs. Where available, we find our photometry is completely consistent with published values in S. D. Van Dyk et al. (2023). We present the PSF photometry of the detected source in Table 2 for SN 2017eaw. All UV, optical, and NIR magnitudes are reported in Vega magnitudes.

2.3. MMT Optical and NIR Imaging

Additionally, we report optical and NIR ground-based photometry of SN 2017eaw. We present *r*- and *i*-band imaging of SN 2017eaw from 2023 September 16 and 18 (60203.144 and 60205.257 MJD), respectively, taken with the Binospec instrument on the MMT (D. Fabricant et al. 2019), and NIR *JHK* photometric observations of SN 2017eaw taken with the MMT and Magellan Infrared Spectrograph (MMIRS) on the MMT (B. McLeod et al. 2012) in Spring 2023 and 2023 December.

For Binospec observations, we utilize a standard dither pattern. These images are then reduced using a custom Python Binospec imaging reduction pipeline, ¹⁹ which does standard flat-fielding, sky background estimation, astrometric alignments, and stacking of the final individual exposures.

For MMIRS, each observation consisted of a dithered sequence which alternates between the target field and a offgalaxy field to allow for better sky subtraction given the infrared-brightness of NGC 6946. The resulting *J-*, *H-*, and *K*-band observations were reduced using a custom pipeline²⁰

which does standard dark-current correction, flat-fielding, sky background estimation and subtraction, astrometric alignments, and stacking of the final individual exposures.

The total field-of-view (FOV) of MMIRS (6.9×6.9) and Binospec (two 8'×15' FOVs with 3' gap) is large enough to calibrate photometric zero-points using isolated stars with cataloged Two Micron All Sky Survey (2MASS; M. F. Skrutskie et al. 2006) and Panoramic Survey Telescope and Rapid Response System (Pan-STARRS; K. C. Chambers et al. 2016), respectively. We derive an effective (e)PSF model for each image by fitting bright, isolated stars with the EPSFBuilder tool from the photutils package in Astropy. For all filters where the SN is detected, we then perform PSF-fitting at the location of the target as well as a set of 20 or more stars spread throughout the image. A loworder, two-dimensional polynomial is included in the fit to account for any spatially varying background and avoid overfitting of the stars. To estimate the statistical uncertainty of each flux measurement, we first set the statistical uncertainty per pixel using the rms error of the fit residuals scaled by a factor of the square root of the reduced χ^2 (usually $\gtrsim 1$), and then multiply by the number of "noise pixels" of the ePSF.²¹ We use the set of 2MASS or Pan-STARRS calibration stars to derive aperture corrections $(\lesssim 0.1 \text{ mag in all filters})$ to scale PSF-fitting magnitudes to the images' photometric zero-points. We adopt the statistical flux uncertainty summed in quadrature with the rms error of the stars used in the zero-point and ePSF aperture correction as the total uncertainty in our reported magnitudes. Despite the large FOV of both MMIRS and Binospec, the limited number of isolated 2MASS and Pan-STARRS stars means that the zero-point rms dominates the reported error.

SN 2017eaw was not detected in the MMIRS H-band and K-band images taken on 60044.427 and 60282.092 MJD (2159 and 2397 days postexplosion), respectively. For these observations, we instead report a 5σ limiting magnitude, based off randomly placed background apertures near the location of SN 2017eaw. Optical (converted to Vega magnitudes) and NIR MMT photometry of SN 2017eaw are reported in Table 2.

^a From explosion on 57885.2 MJD (S. D. Van Dyk et al. 2019).

¹⁹ Initially written by K. Paterson and available on GitHub: https://github.com/CIERA-Transients/POTPyRI.

Adapted from the MMIRS imaging pipeline available on github: https://github.com/CIERA-Transients/POTPyRI.

²¹ A derivation of this quantity by F. Masci can be found at: http://web.ipac.caltech.edu/staff/fmasci/home/mystats/noisepix_specs.pdf.

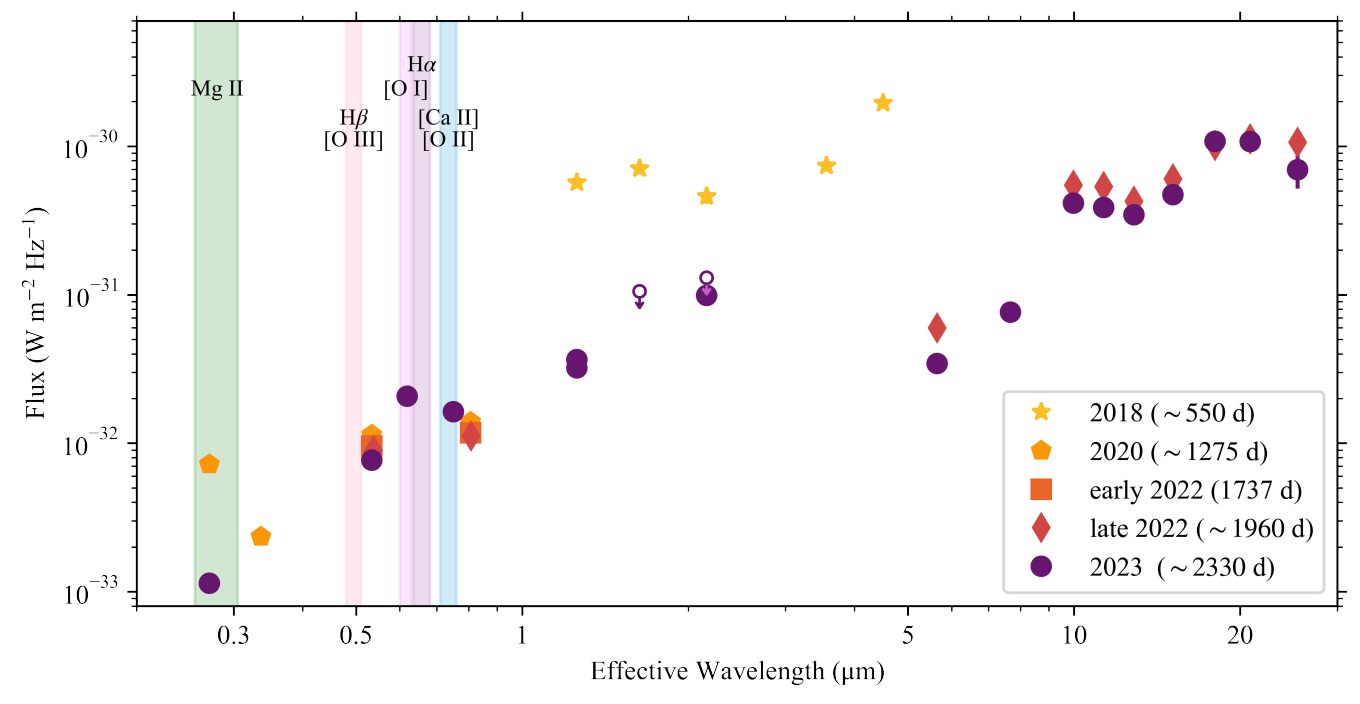


Figure 2. The evolution of the full SED of SN 2017eaw from 2020 to late 2023. The 2018 SED, which includes 3.6 and 4.5 μ m photometry from Spitzer and coincident *JHK* photometry from the the Wide field InfraRed Camera at Palomar Observatory, is also included for reference (S. Tinyanont et al. 2019). Different markers indicate the different epochs, these epochs are defined to include observations taken <6 months from each other, i.e., "late 2022" denotes the second half of the year. Note that the *r*- and *i*-band photometries (purple points at 0.62 and 0.75 μ m) are elevated due to the presence of broad nebular lines, most notably H α , in the filter bandpasses. The flux across all bands <18 μ m has decreased in each consecutive epoch.

2.4. Keck LRIS Spectroscopy

To complement the Cycle 2 JWST MIRI observations, we obtained an optical spectrum of SN 2017eaw on 2024 August 31 (60553.25 MJD, 2668 days postexplosion) using the Low Resolution Imaging Spectrometer (LRIS; J. B. Oke et al. 1995) on Keck I. The spectrum was taken with a 1.5 slit width with the 600/4000 grism and the 400/8500 grating at a central wavelength of 7700 Å and a total exposure time of 7200 s.

The spectrum was reduced in a standard way using LPipe (D. A. Perley 2019). The complete spectrum is further discussed in Section 3.7.

3. Analysis

We present the full time series SED of SN 2017eaw from 2020 to late 2023 in Figure 2. The flux has generally decreased in each consecutive epoch. The notable exceptions to this trend are the r and i bands, where the filter bandpasses include broad hydrogen, calcium, and oxygen lines which have been observed in nebular spectra of SN 2017eaw (see Section 3.7 and M. Shahbandeh et al. 2023). Strikingly, the mid-infrared fluxes blueward of 18 μ m have declined between Cycle 1 and Cycle 2 but are consistent between Cycle 1 and 2 for wavelengths \geqslant 18 μ m. As we discuss in Section 3.1, it is difficult to determine the statistical significance of the SED evolution redward of 15 μ m.

3.1. Comparison with Stars in the Field

To ensure that the observed decrease in luminosity is the result of a true decrease in flux and not the result of changes in the different observing parameters (i.e., exposure time, camera orientation, etc.) used in the Cycle 1 and Cycle 2 observations,

we perform PSF photometry on several stars in the field using methods similar to those used for the SN 2017eaw photometry reported in Table 1.

We first identify infrared bright objects with minimal variability in the field by using the 2MASS catalog (M. F. Skrutskie et al. 2006). These objects are then confirmed to be point sources in all of the JWST filters. Since star clusters may appear as point sources in MIRI filters, we also include a cut to remove any objects in crowded regions by using an HST F814W image of NGC 6946 as a reference. This procedure results in nine comparison stars for the SN 2017eaw field. Given the low signal-to-noise detections of these reference stars, particularly in the redder bands, we opt to do photometry on the stage 3 products for all filters rather than the stage 2 products as was done for SN 2017eaw. We note that stage 2 and 3 photometry of SN 2017eaw produce flux change measurements that are consistent within the uncertainties.

The percent difference in flux between the Cycle 1 (C1) and Cycle 2 (C2) comparison star observations is calculated as (C2–C1)/C1. To determine percent change in the total comparison sample, we calculate the average change across the sample and adopt the standard deviation of the flux values as the error in this measurement.

As shown in Figure 3, we find that the comparison stars are consistent with no change in flux across the two epochs in the F560W, F770W, F1000W, F1130W, F1280W, and F1500W filters. The change in flux is also consistent with zero redward of 15 μ m, with the exception of the F2550W filter. Filters where fewer reference stars are detected have larger errors due to small number statistics. For example, one of the reference stars has a high variance in F560W, resulting in large error bars on the average flux change for this filter. Due to the high

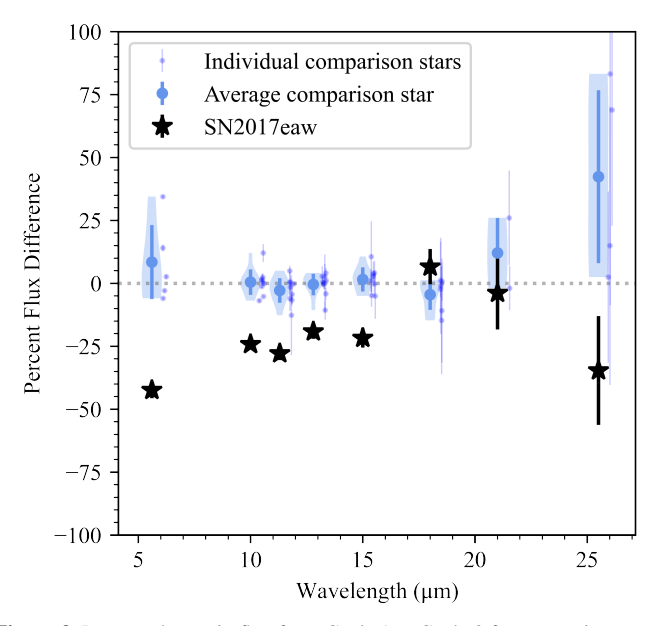


Figure 3. Percent change in flux from Cycle 1 to Cycle 2 for comparison stars in the FOV of SN 2017eaw. The width of the violin plot denotes the number density of comparison stars at a given flux difference, error bars denote one sigma from the average change in flux. For reference, the individual reference stars (small points) are offset \sim 0.5 μ m from the average (large points). The stars in the field are consistent with zero change in flux between epochs for all filters except 25 μ m, though the reddest bands have significant scatter and smaller sample sizes.

 Table 2

 Late Time Optical and NIR Imaging Observations of SN 2017eaw

Filter	MJD	Phase	Vega Mag	Tele/Inst
		(days)		
F336W ^a	59156.290	1271.1	24.28 ± 0.05	HST/WFC3
F275W ^a	59156.389	1271.2	22.75 ± 0.02	HST/WFC3
F555W ^a	59164.831	1279.6	23.77 ± 0.02	HST/WFC3
F814W ^a	59164.813	1279.6	23.12 ± 0.03	HST/WFC3
F555W ^a	59622.265	1737.1	23.96 ± 0.02	HST/WFC3
F814W ^a	59622.259	1737.1	23.30 ± 0.03	HST/WFC3
F555W	59924.463	2039.3	24.02 ± 0.03	HST/ACS
F814W	59924.457	2039.3	23.35 ± 0.02	HST/ACS
F275W	60299.132	2413.9	24.75 ± 0.13	HST/WFC3
F555W	60299.141	2413.9	24.20 ± 0.02	HST/WFC3
K	60040.505	2155.3	19.53 ± 0.10	MMT/MMIRS
J	60044.427	2159.2	21.73 ± 0.09	MMT/MMIRS
H	60044.488	2159.3	>19.96	MMT/MMIRS
J	60282.062	2396.9	21.59 ± 0.19	MMT/MMIRS
K	60282.092	2396.9	>19.23	MMT/MMIRS
r^{b}	60203.144	2317.9	22.95 ± 0.06	MMT/Binospec
$i^{\mathbf{b}}$	60205.257	2320.1	23.00 ± 0.10	MMT/Binospec

Notes.

(This table is available in machine-readable form in the online article.)

sky flux in the redder bands (\geq 18 μ m), there are significant errors in flux measurements for individual stars, large scatter between stars, and smaller sample sizes because few of our reference stars are detectable in the reddest bands. Therefore, we cannot make a high significance measurement of the extent of flux change in SN 2017eaw redward of 15 μ m.

3.2. Decrease in UV Flux

HST F275W and F336W observations from 2020 indicated that SN 2017eaw was UV bright. S. D. Van Dyk et al. (2023) suggested the elevated UV flux was the result of CSM–ejecta interaction but could not rule out the possibility of an underlying UV source, such as an O-star or small stellar cluster. As shown in Figure 2, the F275W observations taken in late 2023 reveal that, while the UV is still elevated, it has declined significantly. The F275W flux in 2023 is 16% of the F275W flux in 2020. Such a significant UV evolution is unlikely to be caused by an underlying star cluster or main sequence star.

It is notable that the F275W filter is particularly sensitive to CSM–ejecta interaction given that it includes the Mg II $\lambda\lambda2796$, 2803 doublet (L. Dessart et al. 2023). Boxy H α emission lines, a signature of late-time CSM interaction, have been observed in the optical spectra of SN 2017eaw since 900 days postexplosion (K. E. Weil et al. 2020), well before the 2020 F275W observations, and boxy H α is still present in more recent spectra (see Section 3.7). Given the evolution and additional observational signatures, the UV evolution is very likely tracing the CSM–ejecta interaction.

3.3. Progenitor Disappearance

Given the proximity of the host galaxy, numerous images of the progenitor of SN 2017eaw were taken by both ground and space-based observatories. HST and Spitzer images identified the progenitor as a 12–15 M_{\odot} dusty red supergiant (C. D. Kilpatrick & R. J. Foley 2018; L. Rui et al. 2019; S. D. Van Dyk et al. 2019). Since the SN explosion, several epochs of HST photometry have been acquired. An analysis of the postexplosion imaging up to 2022 February suggested that the F814W flux had faded below the progenitor level (S. D. Van Dyk et al. 2023).

A further epoch of F814W imaging was obtained in 2022 December and we find it is similarly below the progenitor flux. Additionally, we compare the NIR progenitor flux to the MMT/MMIRS photometry from 2023 December. As shown in Figure 4, we find that the J- and K-band detections are >2 mag fainter than the progenitor. We are therefore able to confirm the progenitor's identification and verify that it has significantly faded from pre-SN observations.

3.4. Dust Modeling Methods

We assume the mid-infrared flux observed by JWST/MIRI in Cycle 1 and Cycle 2 is due to thermal emission from dust grains in or near the SN ejecta. To model the cool and hot dust components, we employ several analytical dust models using a procedure adapted from G. Hosseinzadeh et al. (2023b).

Given the prominent shape of the silicate feature at $\sim\!10~\mu\mathrm{m}$, the observed dust is unlikely to be optically thick. Therefore, we first fit the dust using an optically thin model as was done in M. Shahbandeh et al. (2023) and S. Zsíros et al. (2024). We also model a dusty sphere (similar to M. Shahbandeh et al. 2023) and a dusty shell motivated by work presented in E. Dwek & R. G. Arendt (2024); for both of these dust models we allow the optical depth to vary. All of the models presented here assume there are two temperature components, as motivated by the shape of the SED, within the same geometry. Details of the luminosity equations for these three models can be found in Appendix B.

^a Previously published in S. D. Van Dyk et al. (2023).

^b AB magnitudes are r: 23.11 \pm 0.06 and i: 23.37 \pm 0.10.

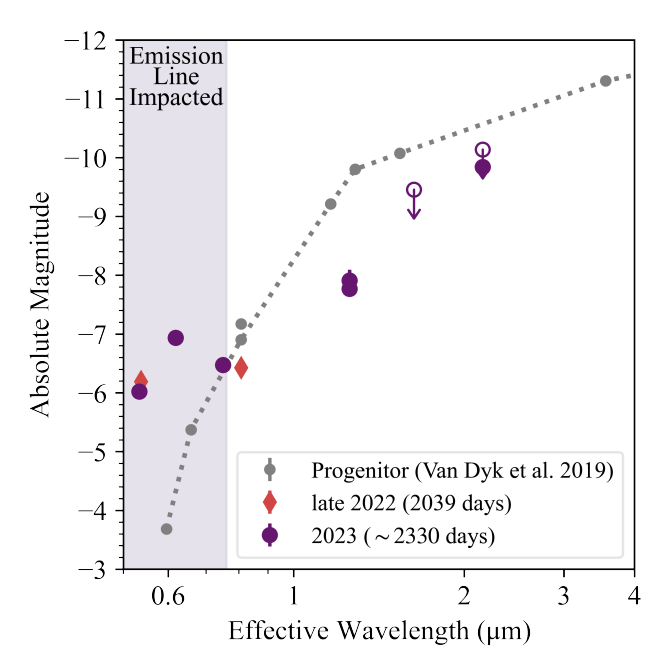


Figure 4. Comparison of optical and NIR observations of SN 2017eaw from 2023 and late 2022 with the progenitor photometry reported in S. D. Van Dyk et al. (2019). *J*- and *K*-band (and F814W to some degree) observations indicate that the SN has faded significantly below the progenitor's level.

We fit all three models (Equations (B3), (B7), and (B12)) to a filter-integrated model of the observed SED using the Markov Chain Monte Carlo routine implemented in the Light Curve Fitting package (G. Hosseinzadeh et al. 2023a). Additionally, we fit an intrinsic scatter term, σ , which inflates the error bars on each photometric data point by a factor of $\sqrt{1+\sigma^2}$, to account for underestimated photometric uncertainties, and to account for uncertainties in the model (e.g., infrared line emission). We run 20 walkers for 2000 steps to reach convergence and then 1000 more steps to properly sample the posterior. All of the optical filters blueward of 0.8 μ m include flux from broad emission lines (see Figure 2), so we exclude all of these filters when fitting the SED. We include only the NIR detections and the JWST/MIRI observations in our fit of the Cycle 2 (2023) SED. For Cycle 1, only the JWST/MIRI observations are considered.

As shown in Figure 2, the 5–25 μ m SED exhibits two distinct peaks with a trough at \sim 13 μ m. This double humped shape is characteristic of optically thin silicate dust. Therefore, we assume that the cool component is silicate dust, with $\rho_{\rm silicate}=3.3~{\rm g~cm^{-3}}$ and $a=0.1~\mu{\rm m}$ as given by A. Laor & B. T. Draine (1993). The composition of the hot component is not as clearly identified. Recent studies report both amorphous carbon and silicate hot dust components around CCSNe (G. Hosseinzadeh et al. 2023b; M. Shahbandeh et al. 2023; S. Zsíros et al. 2024), so we try models with both silicate and amorphous carbon dust ($a=0.1~\mu{\rm m}$ and κ_{ν} from B. T. Draine 1985 and L. Colangeli et al. 1995 for silicate and amorphous carbon, respectively) for the optically thin dust case. For the dusty sphere and dusty shell cases, we assume both components are silicate dust.

We attempt to fit a model of hot amorphous carbon dust and cool silicate optically thin dust, as was done for SN 1980 K (S. Zsíros et al. 2024), to the NIR and JWST/MIRI photometry from Cycle 2. As shown in Figure 5, we find that

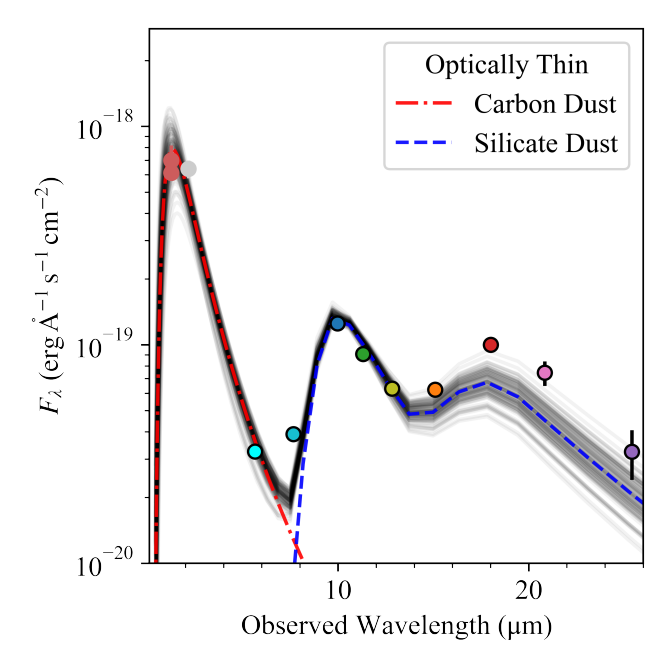


Figure 5. The best-fitting hot amorphous carbon and cool silicate optically thin dust model for the full Cycle 2 infrared SED. Colored points indicate different filters. The carbon+silicate model cannot reproduce the observed flux in the reddest wavelengths and requires temperatures ($T=2200\pm200~{\rm K}$) significantly hotter than the dust condensation temperature to fit the hot dust component.

the carbon+silicate model cannot reproduce the photometry $>15 \mu m$. We note that this excess could potentially be fitted with an additional cooler component, as might be expected of dust formed in the ejecta or pre-existing dust at larger radii. However, given that the SED evolution redward of 15 μ m is not well constrained, we avoid implementing a third dust component. The hot carbon component requires a temperature of $T_{\rm hot} = 2200 \pm 200$ K to reproduce the observed NIR peak, this is significantly above the condensation temperature of amorphous carbon dust ($T \approx 1500$ K; K. Lodders & B. Fegley 1997). We therefore deem it unlikely that the hot dust component in SN 2017eaw is primarily carbonaceous dust. However, we cannot rule out the possibility that there is both carbon and silicate dust in the ejecta, though the shape and temperature of the SED would suggest a high ratio of silicate to carbon dust if carbon dust is present.

Given the poorer quality fit of the carbon+silicate optically thin model, we focus primarily on models where both dust components are silicate. In Table 3, we list the model parameters, their priors, and their best-fit values (median and 1σ equal-tailed credibility interval), for the optically thin, dusty sphere, and dusty shell models of the full considered SED for Cycle 1 and Cycle 2. The best-fit models for all three iterations, and the separate dust components, are shown in Figure 6 (the corresponding corner plots are available in the online journal as a figure set accompanying Figure 7). Since the Cycle 1 SED does not include F770W or NIR observations, we also fit the Cycle 2 SED excluding these filters. For completeness, we also present the results of the Cycle 2 fits excluding the NIR and F770W observations in Table 3 and discuss them further in Appendix C.

 Table 3

 Model Parameters for Dust with Two Silicate Components

			Cycle 1 (~1960 days)	Cycle 2 (~2330 days)	
	Parameter	Priors	All Filters ^a	All Filters ^b	No NIR & F770W ^a
Optically Thin	T _{hot} [kK]	Uniform(1.0, 2.0)	$1.8^{+0.1}_{-0.2}$	1.72 ± 0.03	1.6 ± 0.3
	T _{cool} [kK]	Uniform(0.05, 0.3)	$0.155^{+0.004}_{-0.003}$	0.154 ± 0.002	$0.153^{+0.004}_{-0.005}$
	$M_{ m hot}$ $[M_{\odot}]$	Log-Uniform(1e-15, 1.)	$7.6^{+1.9}_{-0.9} \times 10^{-8}$	$5.4 \pm 0.3 \times 10^{-8}$	$7^{+4}_{-2} \times 10^{-8}$
	${ m M}_{ m cool}$ $[M_{\odot}]$	Log-Uniform(1e-15, 1.)	$7 \pm 1 \times 10^{-4}$	$5.8^{+0.7}_{-0.6} imes 10^{-4}$	$6.1^{+1.6}_{-0.9} \times 10^{-4}$
	Intrinsic scatter	Gaussian(0., 20.)	$2.7^{+0.6}_{-0.4}$	$0.6^{+0.5}_{-0.4}$	$0.4^{+0.5}_{-0.3}$
Dusty Sphere	T _{hot} [kK]	Uniform(0.5, 2.0)	$1.6^{+0.3}_{-0.4}$	1.73 ± 0.04	1.1 ± 0.2
	T _{cool} [kK]	Uniform(0.05, 0.3)	0.163 ± 0.005	$0.158^{+0.003}_{-0.002}$	0.151 ± 0.005
	$M_{ m hot}$ $[M_{\odot}]$	Log-Uniform(1e-15, 0.01)	$1.1^{+1.2}_{-0.3} \times 10^{-7}$	$5.4^{+0.4}_{-0.3} \times 10^{-8}$	$1.3^{+0.9}_{-0.5} \times 10^{-7}$
	${ m M}_{ m cool}$ $[M_{\odot}]$	Log-Uniform(1e-15, 0.01)	$5.2^{+1.1}_{-0.9} \times 10^{-4}$	$5.1 \pm 0.7 \times 10^{-4}$	$7^{+2}_{-1} \times 10^{-4}$
	$R_{\rm outer} \ [10^3 R_{\odot}]$	Log-Uniform(1, 2000.)	700^{+200}_{-100}	1500^{+300}_{-400}	1300^{+500}_{-400}
	Intrinsic scatter	Gaussian(0., 20.)	$1.8^{+0.5}_{-0.4}$	0.8 ± 0.5	$0.4^{+0.5}_{-0.3}$
Dusty Shell	T _{hot} [kK]	Uniform(1.0, 2.0)	1.8 ± 0.1	1.73 ± 0.03	1.3 ± 0.2
	$T_{\rm cool}$ [kK]	Uniform(0.05, 0.3)	$0.158^{+0.003}_{-0.002}$	$0.156^{+0.003}_{-0.002}$	$0.151^{+0.003}_{-0.004}$
	$M_{ m hot}$ $[M_{\odot}]$	Log-Uniform(1e-10, 1.)	$9 \pm 1 \times 10^{-8}$	$5.4 \pm 0.3 \times 10^{-8}$	$9^{+3}_{-2} \times 10^{-8}$
	$M_{\rm cool}$ $[M_{\odot}]$	Log-Uniform(1e-8, 1.)	$5.9^{+0.8}_{-0.5} \times 10^{-4}$	$5.5 \pm 0.7 \times 10^{-4}$	$7 \pm 1 \times 10^{-4}$
	$R_{\rm inner} [10^3 R_{\odot}]$	Log-Uniform(0, 2000.)	<1150	<350	<720
	$R_{\rm outer} \ [10^3 R_{\odot}]$	Log-Uniform(1, 5000.)	1100^{+600}_{-200}	2700^{+1300}_{-900}	3000 ± 1000
	Intrinsic scatter	Gaussian(0., 20.)	$2.1^{+0.6}_{-0.5}$	$0.7^{+0.5}_{-0.4}$	$0.5^{+0.5}_{-0.3}$

Notes

3.5. Dust Modeling Results

Two silicate dust components are able to reproduce the complete SED for all three model geometries, as shown in Figure 6 (top: optically thin, middle: dusty sphere, bottom: dusty shell). While the F770W observation somewhat reduces the spread in the posterior distribution and constrains the hot dust component, the NIR photometry is the most significant factor in constraining the dust models given that the hot dust SED peaks near the effective wavelength of the J filter. The particular dust model is not a significant factor in constraining the dust properties, all the models agree on the masses ($\sim 5.5 \times 10^{-4} M_{\odot}$ for the cool and $\sim 5.4 \times 10^{-8} M_{\odot}$ for the hot dust) and temperatures (~ 160 K for the cool and ~ 1700 K for the hot) of the components for either epoch. The inner radius in the dusty shell model is consistent with zero (i.e., a dusty sphere) for both Cycle 1 and 2 observations. Given this, we report the 3σ upper limit on $R_{\rm inner}$ in Table 3.

When we compare the Cycle 1 to the Cycle 2 full filter set models, we find that all of the best-fit values are consistent within error with the exception of the $\leq 3\sigma$ differences in $M_{\rm hot}$ (mass of hot dust component) for all three model geometries and $R_{\rm outer}$ for the dusty sphere model and dusty shell models. Given that the shape of the SED does not significantly change between Cycle 1 and Cycle 2, it is not unexpected that the temperatures of the dust components are roughly the same between epochs. If the dust is in the SN ejecta or pre-existing and actively interacting with the ejecta, we would expect some increase in the dust radius as the SN ejecta expands over the year between observations. Assuming an ejecta velocity of 7000 km s⁻¹ (an upper estimate from the most recent spectrum, see Figure 8) in the 370 days between the Cycle 1

and Cycle 2 observations, the ejecta radius should expand $\sim 300 \times 10^3 R_{\odot}$, which, when accounting for errors, is consistent with the evolution between $R_{\rm outer}$ in Cycle 1 and Cycle 2 for the dusty sphere model and dusty shell models.

The difference in $M_{\rm hot}$ between epochs is likely due to the lack of constraints on the hot dust component in Cycle 1. Excluding F770W and the NIR photometry from the Cycle 2 fits produces $M_{\rm hot}$ values consistent with those observed in Cycle 1. This highlights the need for NIR photometry for constraining dust masses, particularly around SNe younger and hotter than SN 2017eaw. We note that there is no clear indication, in any of the three models, that the mass of the hot or cool dust components increased in the year between observations.

The Cycle 1 JWST observations were previously modeled for the optically thin and dusty sphere case in M. Shahbandeh et al. (2023). M. Shahbandeh et al. (2023) report only a total dust mass rather than separate mass components as we do here. However, we are able to reproduce all of the dust properties for the dusty sphere of silicate dust case reported in M. Shahbandeh et al. (2023) by assuming $M_{\rm tot} = M_{\rm hot} + M_{\rm cool} \approx M_{\rm cool}$ since $M_{
m hot} \ll M_{
m cool}.$ For the optically thin case, we are unable to replicate the temperature of the hotter dust component as in M. Shahbandeh et al. (2023), though we reproduce the mass of the dust (again assuming $M_{\rm tot} \approx M_{\rm cool}$). However, we find that our Cycle 1 T_{hot} value is consistent within error with our Cycle 2 value, which is well constrained by the NIR data. We note that there are no NIR spectra of SN 2017eaw at this epoch, and therefore we cannot separate the SN's NIR line emission from the hot dust emission. Given this, the temperature of the hot dust component in our Cycle 2 models should be considered an upper limit.

^a Includes same filters as Cycle 1—full JWST/MIRI filter suite excluding F770W.

^b Includes J and K in addition to full JWST/MIRI filter suite.

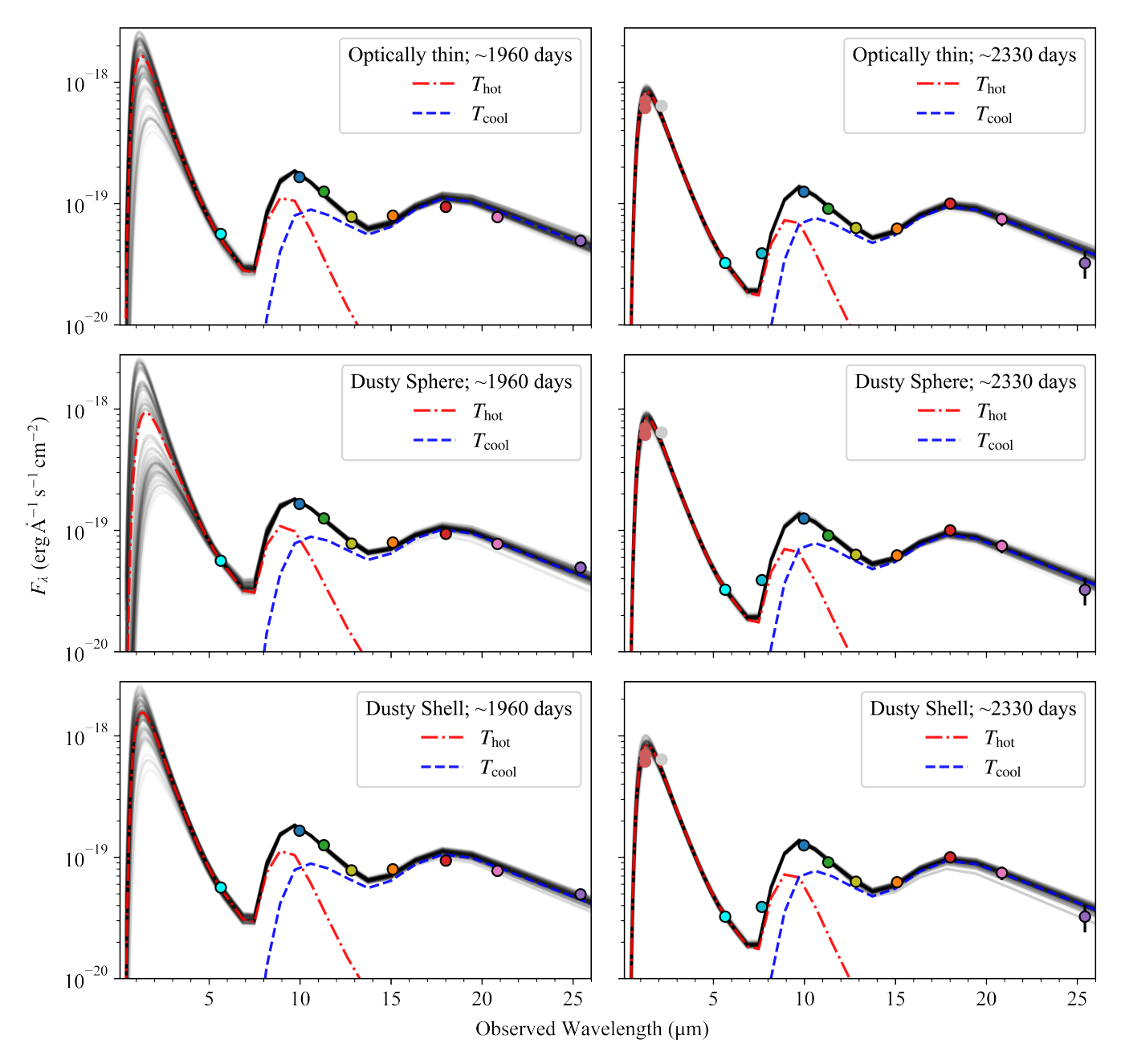


Figure 6. The best-fitting double silicate dust models for the full Cycle 1 and Cycle 2 infrared SEDs for the optically thin, dusty sphere, and dusty shell models. All three geometries are able to reproduce the observed SED. Note that the addition of NIR photometry significantly constrains the hotter dust component of the Cycle 2 dust. A complete figure set of corner plots for these models is available (see Figure 7).

3.6. Dust Geometry

One of the primary ways to distinguish between newly formed and pre-existing dust is to compare the geometry of the dust shell to that of the ejecta. The majority of the pre-existing dust will not survive the interaction with the forward shock and ejecta, and therefore cannot be located within the ejecta. Therefore, if the dust shell is at a radius sufficiently interior to the outermost ejecta, the dust must be newly formed. Similarly, if the dust is outside the outermost radius of the ejecta, then it must be pre-existing.

First, to determine the robustness of any modeled dust radii measurements, we apply the same check as S. Zsíros et al. (2024) and calculate the optical depth as follows

(L. B. Lucy et al. 1989):

$$\tau = \kappa_{\text{average}} \frac{M_{\text{dust}}}{4\pi r^2},\tag{1}$$

where $\kappa_{\rm average} = 750~{\rm cm}^2~{\rm g}^{-1}$ estimated for 0.1 $\mu{\rm m}$ silicate dust (from grain properties in B. T. Draine & A. Li 2007; A. Sarangi 2022). In the case of optically thin dust, the minimum outer radius of the dust is set by the blackbody radius. The dusty sphere case produces the minimum blackbody radius, which is $R_{\rm BB} = 3.39 \times 10^5 R_{\odot}$ and $3.05 \times 10^5 R_{\odot}$ for Cycle 1 and Cycle 2, respectively. If we assume this radius and a total dust mass of $5.4 \times 10^{-4} M_{\odot}$ (based on the dust mass from the optically thin dust model), Equation (1) gives

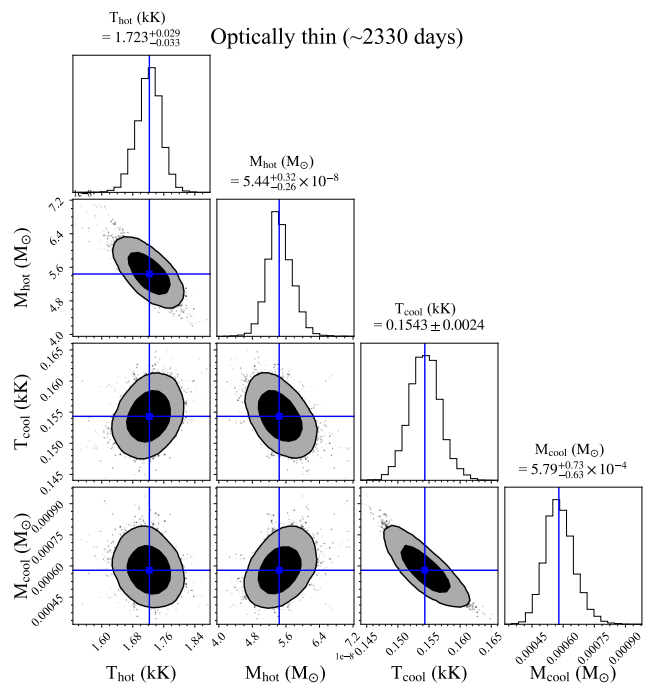


Figure 7. The corner plot for the Cycle 2 optically thin dust model. All six corner plots corresponding to the SEDs displayed in Figure 6 are available as a figure set in the online journal.

(The data used to create this figure are available in the online article.) (The complete figure set (6 images) is available in the online article.)

$\tau=0.1.$ Therefore, the observable dust around SN 2017eaw may be optically thin.

We find the quality of the optically thin model fit to be comparable to that of the dusty sphere and dusty shell model fits for both epochs, further indicating that the dust may be optically thin. We also find that the dusty shell model converges in the case where the outer radius is set to be inside the ejecta radius $(2 \times 10^6 R_{\odot}$, i.e., the radius at 2300 days assuming a velocity of 7000 km s⁻¹) and also does so when the inner radius is set to be greater than the ejecta radius. Both of these scenarios result in similar dust masses and temperatures for both dust components. We, therefore, assume that the dust is optically thin enough that the radius of the dust cannot be well constrained. Nevertheless, we compare the measured dust radii in the dusty sphere and shell models to the ejecta for completeness.

The radius at which dust resides in the ejecta is often quoted as a velocity coordinate with respect to the ejecta in order to account for the fact that the ejecta, and anything within it, is expanding over time. The outer edge of the ejecta is at a velocity of \sim 7000 km s⁻¹, given that the line profiles in the 1811 and 2888 days nebular spectra indicate the outermost ejecta is interacting with CSM at this radius (see Section 3.7 and M. Shahbandeh et al. 2023). To determine the velocity coordinate of the dust, we assume the simplest case R = vt, where t is the time since explosion, R is the radius of the dust, and v is the velocity. If we use the radius derived from the dusty sphere model (since $R_{\rm sphere} < R_{\rm outer, shell}$), we find that the velocity coordinate of the dust emission is 2900^{+800}_{-400} km s⁻¹ and 5000 ± 1000 km s⁻¹ in Cycle 1 ($t \sim 1960$ days) and Cycle 2 ($t \sim 2330$ days), respectively.

The radius within which dust formation can begin is the subject of debate. Recent work by A. Sarangi (2022) suggests dust formation is confined to the 2500 km s⁻¹ velocity

coordinate, at least for the first 3000 days. Other studies have suggested this velocity coordinate may be as high as 5000 km s⁻¹ (J. K. Truelove & C. F. McKee 1999; K. Maguire et al. 2012). If we assume the radius from the dusty sphere model, the Cycle 1 dust component is near the region of the ejecta where dust formation may occur. The Cycle 2 dust component is consistent with dust both inside and outside the ejecta. For the dusty shell model, the velocity coordinates for Cycle 1 and 2 are 4500^{+2500}_{-800} and 9000^{+4000}_{-3000} km s⁻¹, respectively, both of which are consistent with dust located outside of the ejecta. Regardless of model, the radii from the dust modeling could account for both pre-existing and newly formed dust geometries.

3.7. Spectral Evolution

As shown in Figure 8, the nebular spectrum of SN 2017eaw continues to exhibit a prominent broad boxy $H\alpha$ profile, denoting continued CSM-ejecta interaction even at 2668 days after explosion. A boxy H α profile was first observed in SN 2017eaw 900 days postexplosion (K. E. Weil et al. 2020). A comparison of the 2668 and 900 days $H\alpha$ profiles reveals that the center of the 2668 days profile is perhaps somewhat more blueshifted, $-430 \pm 40 \text{ km s}^{-1}$ compared to -160 ± 30 km s⁻¹, with a slightly steeper slope at the top of the line. This shape indicates dust attenuation, since the light from the receding ejecta, i.e., the red side of the line profile, is absorbed by the dust along the line of sight. However, it is difficult to robustly determine the impact of the dust attenuation given the signal-to-noise ratio of the spectrum. The velocity of the ejecta, as measured at the location of full width at half-maximum, has decreased, 8000 km s⁻¹ at 900 days compared to 7000 km s⁻¹ at 2668 days, but some slowing is expected given the extent of the continued CSM interaction (L. Dessart 2024). Ultimately, the H α at 2668 days is remarkably similar to that at 900 days and minimal evolution seems to have occurred in almost 2000 days.

The three most prominent lines in the 2668 days Keck spectrum are $H\alpha$, [O II] $\lambda\lambda7319$, 7330, and [O III] $\lambda5007$. We compare the profiles of these lines in Figure 9. We treat the [O II] doublet as a line centered at 7324.5 Å. A [Ca II] doublet can be present in the [O II] line complex but the calcium doublet is clearly subdominant to the [O II] lines at this epoch. Despite the existence of the [O III] $\lambda\lambda4959$, 5007 doublet, the shape of the line profile in the 2668 days spectrum suggests the majority of the light is from the stronger of the lines, we therefore attribute the entire profile to [O III] $\lambda5007$. The [O III] $\lambda5007$ line complex also contains $H\beta$, which is visible on the blue shoulder. Again, [O III] $\lambda5007$ is the stronger of the two lines. Therefore, we treat the [O II] and [O III] lines as primarily oxygen in our analysis.

The edges of the oxygen profiles line up remarkably well with the edges of the $H\alpha$ profile. The oxygen lines are notably attenuated on the red side of the profile. This effect is less pronounced in the hydrogen line but still seems to be present. This might suggest there is a reservoir of dust inside the ejecta which is absorbing light from the far side of the SN. If this attenuation is due to newly formed dust in the ejecta, rather than some asymmetry in the explosion and/or CSM, the strength of the attenuation and the low dust mass revealed in the JWST/MIRI images suggests that the majority of this interior dust is likely too optically thick to observe in the midinfrared.

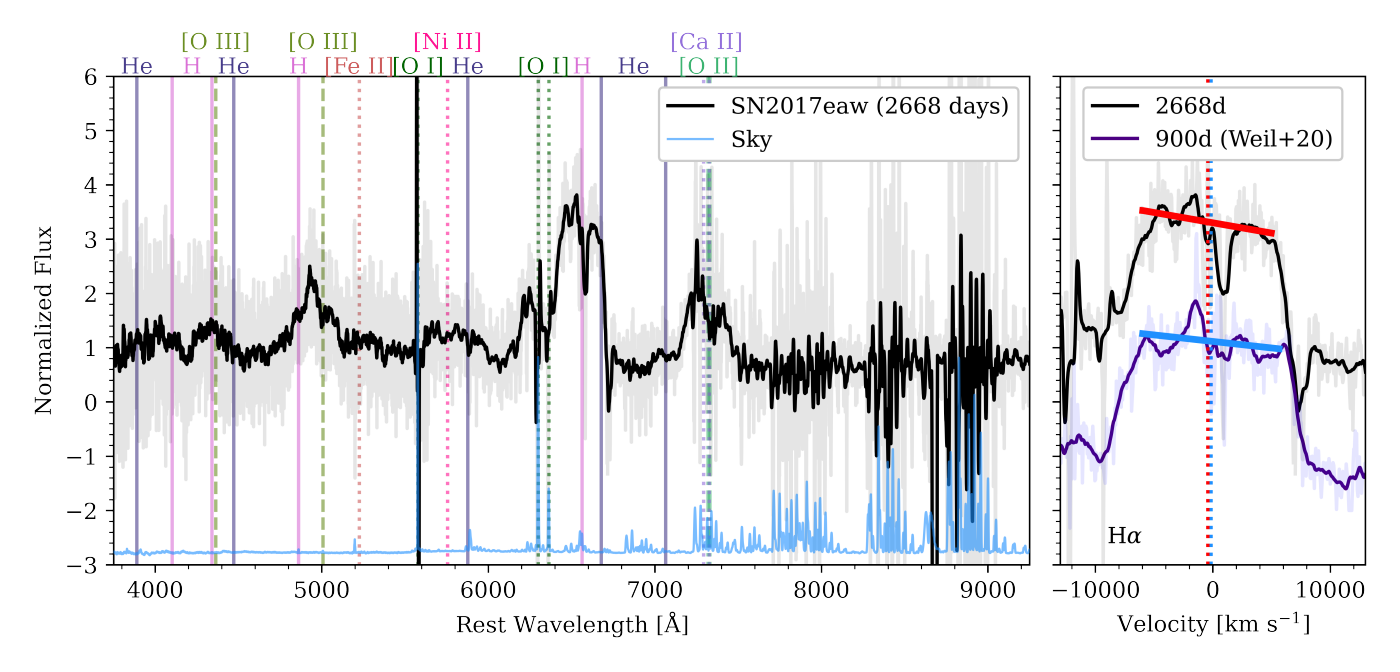


Figure 8. Left: The complete Keck LRIS spectrum taken at 2668 days postexplosion. The spectrum has been smoothed for clarity; the unsmoothed spectrum is displayed at lower opacity. The sky spectrum is shown below the SN 2017eaw spectrum for reference. Right: The H α profile of the most recent Keck spectrum compared to the 900 days spectrum published in K. E. Weil et al. (2020). The solid red and blue lines are a fit to the top of the 2668 and 900 days H α line profiles, respectively. The center of the profiles is marked by a line of the same color.

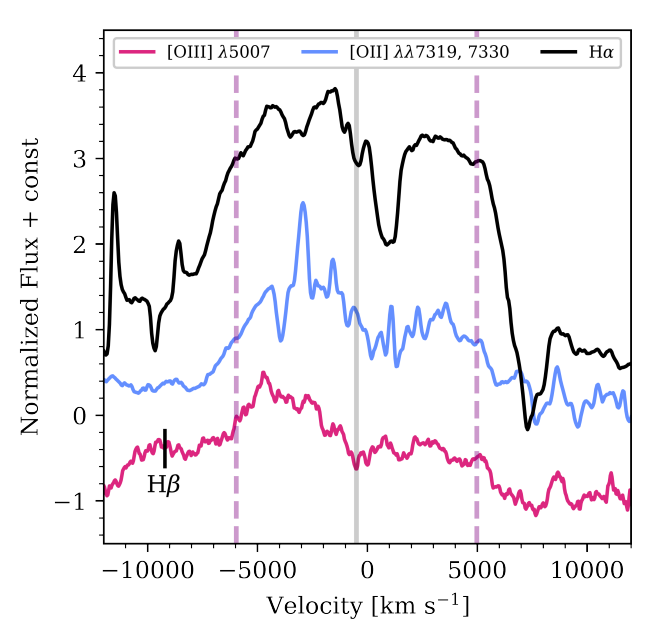


Figure 9. The line profiles of the three most prominent lines in the 2668 days Keck spectrum: [O III] $\lambda 5007$, [O II] $\lambda \lambda 7319,7330$, and H α . The purple dashed lines mark the edges of the top of the boxy H α profile. The gray line marks the center of the H α profile. The spectrum is smoothed for clarity.

Recent work by L. Dessart et al. (2025) presents models of an SN IIP at 1000 days postexplosion that is CSM-interacting and also contains a small mass of dust in the cold dense shell. They find there is no significant dust attenuation effect for dust interior to the ejecta due to the small angle of the inner dust relative to the emitting region of the outer ejecta. Furthermore, in contrast to noninteracting SNe, in the L. Dessart et al. (2025) CSM-interacting SN model the interior dust has no

impact on the line strengths, or the hydrogen-oxygen line ratios, due to the fact that 99.7% of the model emission is from the outer ejecta. Indeed, K. E. Weil et al. (2020) note no significant signs of dust attenuation in SN 2017eaw at 900 days postexplosion. At 2668 days postexplosion, the velocity of the ejecta (7000 km s⁻¹) is similar to that of the 1000 days model (8000 km s⁻¹) in L. Dessart et al. (2025) and it is possible that the observed line attenuation is not due to interior dust. Although this physical picture may still be valid, we caution against direct comparisons given that both the inner and outer regions have evolved for an additional \sim 1700 days. The velocity of the ejecta at 2668 days suggests that the outer regions of the ejecta have somewhat slowed due to CSM interaction and the conclusions from 1000 days may no longer be valid. L. Dessart et al. (2025) also investigate the effect of 10^{-4} , 5×10^{-4} , and $10^{-3} M_{\odot}$ of dust in the ejecta at a velocity coordinate of 8000 km s⁻¹. These models produce H α profiles very similar to the one at 2668 days. The model profiles include a dip in the center (near rest wavelengths) due to the increased optical depth of the limbs of the shell. We refrain from definitively linking a similar feature in the observed $H\alpha$ profile with dust given the low SNR of the spectrum. Further modeling of the effects of dust in CSM-interacting SNe II at late times (>1000 days postexplosion) is needed to understand the evolution of $H\alpha$ and the strongest oxygen lines.

4. Dust Origin Scenarios

Despite the general decrease in mid-infrared flux from Cycle 1 to Cycle 2, the SED evolution of SN 2017eaw points to dust which has not significantly changed in the year between JWST/MIRI observations. Given the optically thin nature of the dust and the constant dust temperatures, this drop in flux could be due to a decline in dust mass. These observations indicate a possible trend to watch for in future observations

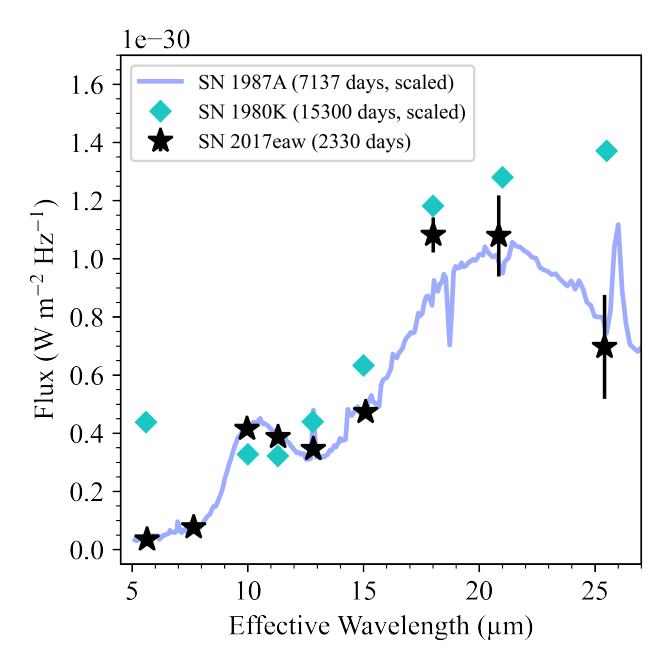


Figure 10. A comparison of SN 2017eaw's mid-infrared SED to the mid-infrared SED of SN 1980K (S. Zsíros et al. 2024) and a Spitzer IRS spectrum of SN 1987A (E. Dwek et al. 2010). The SN 1987A and SN 1980 K data have been scaled to the flux of the SN 2017eaw SED from 10 to 15 μ m. The SN 2017eaw SED is strikingly similar, particularly to that of SN 1987A at 6000–8000 days. The mid-infrared flux during this epoch of SN 1987A's evolution is likely due to cool pre-existing dust collisionally heated by the strong interaction between the SN ejecta and the equatorial ring (R. G. Arendt et al. 2016).

and set a robust baseline against which future measurements can be compared. Even if the dust mass is not decreasing, it has not increased as might be expected if dust formation was actively occurring. Furthermore, the lack of temperature evolution indicates that the mass of any newly formed dust that cooled between the JWST observations is small compared to the total dust mass observable in the mid-infrared.

As was noted in M. Shahbandeh et al. (2023), even the cooler component of dust is too warm to be heated only by the ejecta of SN 2017eaw. The observed dust temperatures require an external heating mechanism to be present. Given that neither of the components have cooled or heated markedly since the initial observations reported in M. Shahbandeh et al. (2023), the external heating mechanism must be maintained over the course of the year between observations. The possible heating mechanisms depend on the location of the dust, and can therefore be used to probe the dust origin. We explore three different scenarios where the mid-infrared dust is primarily (1) pre-existing in the CSM and collisionally heated, (2) pre-existing and radiatively heated, and (3) newly formed in the ejecta and radiatively heated.

4.1. Collisionally Heated Pre-existing Dust

The mid-infrared SED of SN 2017eaw is somewhat similar in shape to that of SNe 1987A and 1980K at significantly later phases, see Figure 10. In the case of both SNe 1987A and 1980K, the 8–20 μm emission is consistent with 150–180 K silicate dust, remarkably similar to SN 2017eaw. Notably the mid-infrared flux in SN 2017eaw, which is primarily dominated by the cool dust component, is almost identical in shape to Spitzer IRS spectra of SN 1987A between 6000 and

8000 days postexplosion. This component in SN 1987A has been linked to the collisional heating of the equatorial ring (E. Dwek et al. 2010; R. G. Arendt et al. 2016, 2020), and a similar scenario was suggested for SN 1980K (S. Zsíros et al. 2024). The mass of dust in the $\sim\!160\,\mathrm{K}$ component of SN 2017eaw is $\sim\!1$ order of magnitude larger than observed in SN 1987A and $\sim\!1$ order of magnitude smaller than observed in SN 1980K.

To determine if it is plausible for the cooler component of SN 2017eaw's mid-infrared dust to be collisionally heated via interaction between the ejecta and CSM, we follow the method of O. D. Fox et al. (2010) for estimating the mass of dust processed by the forward shock (see also O. D. Fox et al. 2011; S. Tinyanont et al. 2016; S. Zsíros et al. 2022, 2024). Any pre-existing dust must reside outside the evaporation radius, inside which the peak luminosity of the SN will have destroyed any pre-existing dust grains. Assuming the temperature and peak bolometric luminosity measured by T. Szalai et al. (2019a), 14,000 K and $\sim 10^{43}$ erg s⁻¹ (rounded from $L_{\rm peak} \approx 7 \times 10^{42}$ erg s⁻¹), respectively, the evaporation radius ($R_{\rm evap}$) is $2.7 \times 10^4 R_{\odot}$. $R_{\rm evap}$ is significantly less than the ejecta radius at 2000 days. In both JWST epochs, the SN ejecta has far surpassed the evaporation radius and could feasibly be interacting with CSM containing pre-existing dust.

In the case of collisional heating, the hot, postshocked gas heats a shell of pre-existing dust. The total mass of this dust can be determined from the volume of the emitting shell using equations for grain sputtering and by assuming a dust-to-gas ratio of 0.01 (O. D. Fox et al. 2010). This gives

$$\frac{M_{\text{dust}}}{M_{\odot}} \approx 0.0028 \left(\frac{\nu_{\text{s}}}{15,000 \text{ km} \text{ s}^{-1}}\right)^3 \left(\frac{t}{\text{year}}\right)^2 \left(\frac{a}{\mu \text{m}}\right),$$
 (2)

where $\nu_{\rm s}$ is the shock velocity, t is the time since explosion, and a is the dust grain size. Similar to S. Zsíros et al. (2024), we use $\nu_{\rm s}=5000~{\rm km~s^{-1}}$ and $15{,}000~{\rm km~s^{-1}}$ and a=0.005 and $0.1~\mu{\rm m}$ (we assume $a=0.1~\mu{\rm m}$ in our dust modeling) as our lower and upper bounds, respectively. Assuming these values, the range of dust masses that could be collisionally heated is $\sim 10^{-5} - 10^{-2} \, M_{\odot}$. The total dust masses observed in both Cycle 1 and 2 are in the middle of this range. We note that the velocity of the ejecta measured from the nebular spectra, 7000 km s⁻¹, with a 0.1 $\mu{\rm m}$ dust grain could result in a collisionally heated dust mass of $10^{-3} \, M_{\odot}$. This result suggests that the majority of the dust observed in the mid-infrared could reasonably be collisionally heated pre-existing dust.

The correlation between the UV and mid-infrared flux evolution might also suggest the observed dust is collisionally heated. As shown in Figure 11, the flux in F275W decreased 27% per year between 2020 and 2023. Similarly, the MIRI flux decreased an average of 21% ($\pm 15\%$) per year across all filters between the Cycle 1 (2022) and Cycle 2 (2023) observations. The F275W filter notably includes Mg II $\lambda\lambda$ 2796, 2803, one of the UV features most strongly affected by CSM interaction (L. Dessart et al. 2023). Therefore, the evolution in F275W can be used as a proxy for the extent of CSM. The drop in F275W flux and corresponding drop in the mid-infrared suggests that both wavelength regimes are probing the same medium. This correlation between UV and mid-infrared flux is similar to the X-ray (which similarly probes CSM interaction) and midinfrared evolution observed in SN 1987A at 6000-8000 days, during which the infrared-to-X-ray flux ratio remains constant.

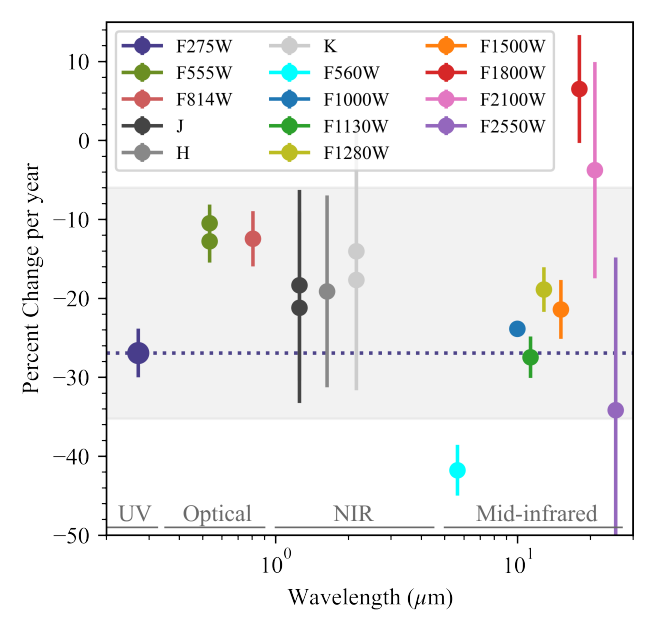


Figure 11. The percent change in flux per year for SN 2017eaw. The UV flux of SN 2017eaw decreased from 2020 to 2023, indicating that the observed UV excess is likely the result of CSM interaction rather than an underlying star or stellar population. The gray region denotes 1 standard deviation from average mid-infrared flux change, this lines up well with the observed decrease in both the NIR and UV (also plotted as a navy dotted line for reference). This suggests the mid-infrared, NIR, and UV are probing a similar region of the SN ejecta.

As shown in Figure 10, the mid-infrared SED of SN 2017eaw is nearly identical to that of SN 1987A during this epoch where the $8-20~\mu m$ dust component is believed to be collisionally heated dust in the equatorial ring (E. Dwek et al. 2010; R. G. Arendt et al. 2016).

Furthermore, the reduction in UV flux does not correlate with a change in the temperature of the dust. If the dust, whether pre-existing or newly formed, is radiatively heated by CSM interaction, the temperature of the dust is expected to decrease with the UV flux, and therefore CSM interaction. There is no evidence of the majority of the mid-infrared dust cooling between epochs.

4.2. Radiatively Heated Pre-existing Dust

The theory that the cool dust component is collisionally heated assumes a linear decline in UV luminosity from 2020 to 2023, but there is no UV data between these epochs to track the decline. It is possible that the UV luminosity was constant enough in the year between the JWST/MIRI observations for the dust temperature to not substantially change over the course of the year. In this scenario, radiative heating could still account for the lack of temperature evolution in the dust. The decrease in mid-infrared flux could be attributed to a changing geometry of the dust shell illuminated by the CSM interaction. We therefore cannot use the similar UV and mid-infrared decline rates to completely rule out the possibility of radiative heating.

A simple infrared echo model, assuming the light from the SN explosion excites pre-existing dust, places the echo radius at $R_{\rm echo} = ct_{\rm echo}/2$, where $t_{\rm echo}$ is the duration of the light echo (M. F. Bode & A. Evans 1980; E. Dwek 1983). Assuming a lower limit of $t_{\rm echo} = 2330$ days in order for the echo to still be detectable in the Cycle 2 mid-infrared observations, this gives

 $R_{\rm echo}=4.3\times10^7\,R_{\odot}$, significantly above the outer dust radii given by the nonoptically thin models in Section 3.4. When the ejecta is between the evaporation and the light echo radii, as is the case for SN 2017eaw, the luminosity from CSM–ejecta interaction heats the pre-existing grains, creating a CSM echo (O. D. Fox et al. 2010, 2011).²² M. Shahbandeh et al. (2023) found that for SN 2017eaw, the optical luminosity necessary to heat the grains to the temperature of the cool dust component in the Cycle 1 data exceeds the observed optical luminosity. Unsurprisingly, we find this to be the case for the Cycle 2 dust as well.

However, L. Dessart & D. J. Hillier (2022) suggests that CSM–ejecta interaction may primarily produce UV emission, especially in Ly α and Mg II $\lambda\lambda$ 2796, 2803. Assuming constant luminosity across the UV (10–400 nm), we use the F275W observation to estimate $L_{\rm UV}=3\times10^5\,L_{\odot}$ in 2023. This may be an overestimation of the total UV luminosity given the Mg II lines fall into the F275W filter. Nevertheless, this value is similar to the $\sim10^5\,L_{\odot}$ modeled in L. Dessart & D. J. Hillier (2022), indicating that the UV luminosity could account for the temperature of the observed mid-infrared dust. More extensive wavelength coverage in the UV is required to place robust limits on the UV luminosity.

4.3. Newly Formed Dust

Pre-existing dust does not preclude the existence of newly formed dust in the ejecta. The detection of CO in the ejecta between 200 and 500 days postexplosion indicates that the ejecta has long been cool enough to form dust (S. Tinyanont et al. 2019). Furthermore, there are signs of blueshifted line profiles in the spectra at roughly 2000 days (just before the JWST Cycle 1 observations) (M. Shahbandeh et al. 2023) and at 2668 days (as discussed in Section 3.7). The observed dust attenuation in the red side of the line profiles suggests there is dust in the ejecta of the SN.

The optical spectra of SN 2017eaw indicate that the SN is producing dust (although see L. Dessart et al. 2025). However, the newly formed dust might be too optically thick to be observed in the mid-infrared, even at >2000 days postexplosion. In this case, only thermal emission from the outermost shell of the total mass of newly formed dust will be observable. This outermost layer would only constitute an extremely small percentage of the total newly formed dust mass and may not noticeably change the mid-infrared SED if a more massive amount of pre-existing dust is also present. Nevertheless, geometrical arguments (see Section 3.6) indicate that some of the observed mid-infrared dust could be located within the ejecta or in a cold dense shell between the forward and reverse shock. Given the optical depth and evolution of the cool dust component, it is unlikely to be primarily newly formed, though some component of this dust may be.

In contrast, there are minimal constraints on the evolution of the hot dust component due to the lack of NIR observations during Cycle 1, and there may have been dust growth and/or cooling between the Cycle 1 and 2 observations as would be expected of a newly formed dust component. There are no NIR spectra of SN 2017eaw at this late epoch, so we are unable to quantify the extent to which the NIR emission is from the SN itself rather than dust. NIR spectra of SN 1987A at around 2000 days shows strong emission lines in *J* band but none in *K*

²² Sometimes referred to as a circumstellar shock echo.

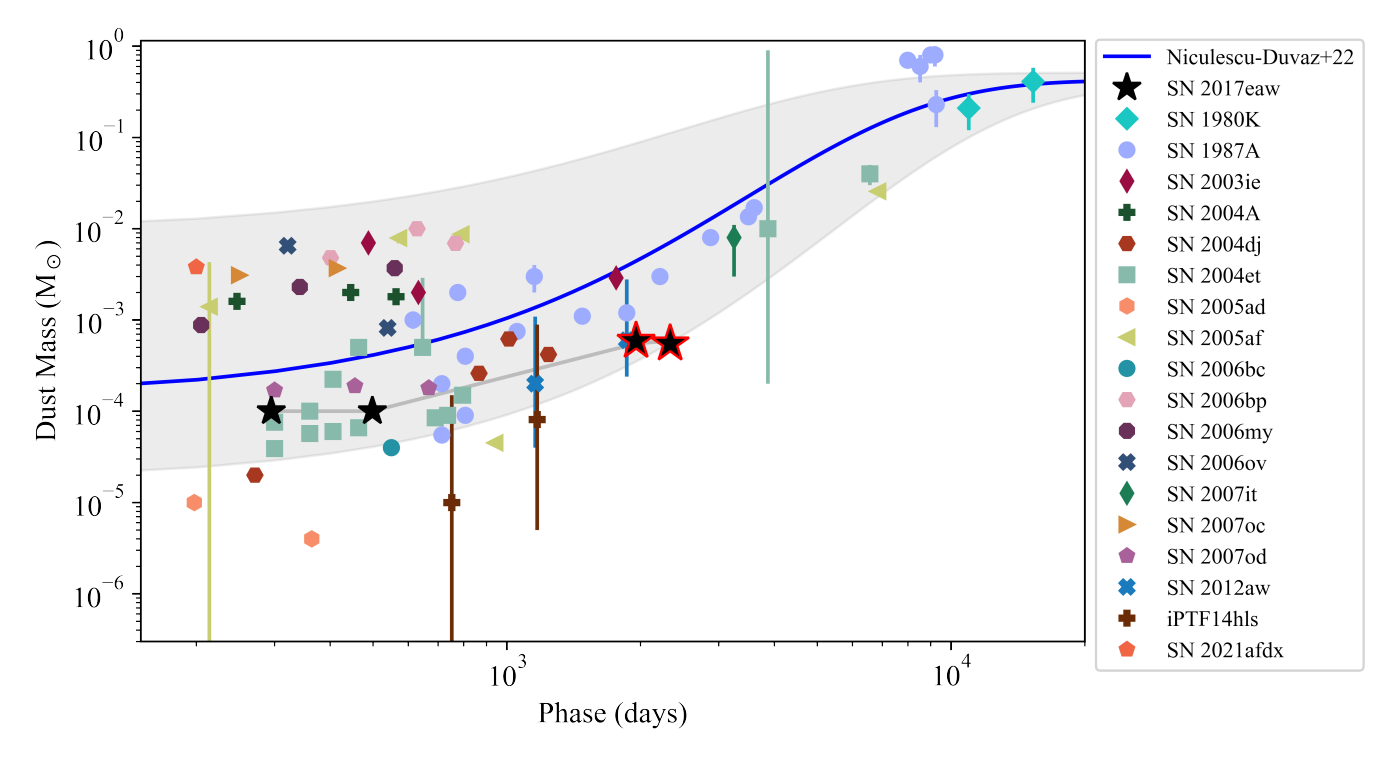


Figure 12. Dust mass vs. time for a collection of Type II CCSNe. Dust masses for SN 2017eaw derived in this work (red-edged black stars) do not significantly differ from the dust production trend presented in M. Niculescu-Duvaz et al. (2022, their Figure 23) denoted by the blue line and gray shaded region. SN dust measurements in this figure include SN 2017eaw (S. Tinyanont et al. 2019), SN 1980K (A. Bevan et al. 2017; S. Zsíros et al. 2024), SN 1987A (M. Matsuura et al. 2011, 2015; R. Indebetouw et al. 2014; R. Wesson et al. 2015; A. Bevan & M. J. Barlow 2016), SN 2003ie (T. Szalai & J. Vinkó 2013), SN 2004dj (T. Szalai et al. 2011), SN 2004et (R. Kotak et al. 2009; J. Fabbri et al. 2011; M. Niculescu-Duvaz et al. 2022; M. Shahbandeh (T. Szalai & J. Vinkó 2013), SN 2005ad (T. Szalai & J. Vinkó 2013), SN 2005ad (T. Szalai & J. Vinkó 2013), SN 2005bp (T. Szalai & J. Vinkó 2013), SN 2006my (T. Szalai & J. Vinkó 2013), SN 2007bc (T. Szalai & J. Vinkó 2013), SN 2007oc (T. Szalai & J. Vinkó 2013), SN 2007od (J. E. Andrews et al. 2010), SN 2012aw (M. Niculescu-Duvaz et al. 2023), iPTF14hls (M. Niculescu-Duvaz et al. 2023), and SN 2021afdx (G. Hosseinzadeh et al. 2023b).

band (A. Fassia et al. 2002). If this is also the case for SN 2017eaw, the hot dust component could be slightly cooler than modeled. Furthermore, there is likely some flux in this component that is due to blackbody emission from the SN. Our inferred cool dust mass of $5.4 \times 10^{-8} \, M_{\odot}$ (see Table 3) should be treated as an upper limit of the amount of dust found in the hot component. Given the small amount dust in the hot component (relative to the cold component), this uncertainty does not impact the conclusions of this work. Ultimately, we are unable to confirm the origin of the hot dust component from the existing observations. Further observations of SN 2017eaw should also include NIR observations to place constraints on the evolution of the hot component and provide insights into its origin.

4.4. Implications for Dust Formation in CCSNe

Significant work has been done to understand the timeline of dust formation in CCSNe. When SN 2017eaw's mid-infrared dust mass is compared to literature values of CCSNe dust masses, it lies near the lower limit of the dust trend observed in M. Niculescu-Duvaz et al. (2022), as shown in Figure 12. The slight fluctuation in dust mass from $\sim\!2000$ to $\sim\!2300$ days postexplosion is similar to trends observed in several other SNe, though this behavior has never been observed in another SN $>\!2000$ days postexplosion. However, SN 2017eaw is the only SN other than SN 1987A with multiple epochs of midinfrared observations between 1000 and 5000 days postexplosion.

If the mid-infrared dust emission in SN 2017eaw is primarily due to pre-existing dust, then its location on the dust formation timeline may be significantly different than shown in Figure 12. It is possible that many of the early time mid-infrared dust measurements of CCSNe are similarly contaminated with pre-existing dust. Late-time dust mass measurements of SN 1987A were done in the far-infrared and submillimeter and probed dust significantly colder than can be observed with JWST (M. Matsuura et al. 2011, 2015; R. Indebetouw et al. 2014). For SN 1980 K, reported dust measurements were measured by modeling the dust attenuation on optical spectral lines. The mid-infrared SED of SN 1980 K reveals 100 times less dust than indicated by the line profiles (S. Zsíros et al. 2024). This suggests that the majority of the dust in SN 1980 K is also too cold to be observed by JWST/MIRI. The same might be true for SN 2017eaw but the signal-to-noise ratio of the recent spectra makes modeling of the line profiles difficult.

However, SN 2017eaw is significantly younger than both SN 1980 K and SN 1987A. Any newly formed dust around SN 2017eaw should be more optically thick than observed in the two older SNe. In the case of optically thick dust, radiative processes from CSM-ejecta interaction will only heat the outermost shell of newly formed dust, which is likely to make up only a tiny amount of the total dust mass. Over the course of a year, the expansion of a shell of newly formed dust may not be enough to visibly evolve the mid-infrared SED.

5. Summary and Conclusion

We present late-time UV, optical, and NIR observations of SN 2017eaw to map its spectral energy evolution. The SN has declined in flux across almost all wavelengths. We find that the NIR flux has declined below the progenitor level, confirming the progenitor's detection. SN 2017eaw is still detected in HST WFC3/UVIS F275W, and the optical spectrum at 2668 days exhibits broad boxy line profiles, particularly $H\alpha$, indicating that there is continued CSM–ejecta interaction, even at >2500 days postexplosion.

SN 2017eaw is one of the first SNe to have multiepoch JWST MIRI imaging. These observations reveal that the mid-infrared flux has decreased in most filters in the year between the MIRI observations. SED modeling reveals a hot (\sim 1700 K) silicate dust component of 5.4 \times 10⁻⁸ M_{\odot} and a cool (\sim 160 K) silicate dust component of 5.5 \times 10⁻⁴ M_{\odot} consistent with being optically thin. Here, we cite the dust modeling values for the dusty shell case since these values are between the optically thin and dusty sphere models. Interestingly, there is no indication that the dust is cooling or increasing in mass, as might be expected for dust which is actively forming.

Furthermore, the decline in mid-infrared flux is similar to that observed in the UV, perhaps hinting that the dust observed in the mid-infrared is located in the same CSM whose interaction with the ejecta is producing UV flux. The evolution in the UV suggests a changing CSM density or geometry around SN 2017eaw. To understand how this continues to affect the dust budget and the dust heating mechanism, continued X-ray and UV observations are necessary.

The multiwavelength evolution of SN 2017eaw suggest that, while there may be newly formed dust in the ejecta or cold dense shell, a significant fraction of the cool dust observed in the mid-infrared is likely pre-existing. There is a need for further late time (>1000 days postexplosion) multiwavelength observations for the nearest SNe, such as SN 2017eaw, in order to map the extent and duration of CSM interaction and its impact on dust evolution. Such observations, spanning the UV to the mid-infrared, will reveal insights into red supergiant mass loss in the final years before death and help to constrain the timeline of new dust production in SNe II.

Acknowledgments

We thank R.G. Arendt for providing the Spitzer IRS spectra of SN 1987A. Our thanks go to C. DeCoursey and J. Pierel for their help with JWST photometric reduction using space_phot. We also thank D. Perley for helpful advice in reducing the SN 2017eaw Keck LRIS spectrum.

The complete set of HST and JWST data presented in this article were obtained from the Mikulski Archive for Space Telescopes (MAST) at the Space Telescope Science Institute. The specific observations analyzed can be accessed via doi: 10.17909/tk94-1430.

This work is based in part on observations made with the NASA/ESA/CSA James Webb Space Telescope. The data were obtained from MAST at the Space Telescope Science Institute, which is operated by the Association of Universities for Research in Astronomy, Inc., under NASA contract NAS 5-03127 for JWST. These observations are associated with programs GO 3295 and GO 2666.

This research is based in part on observations made with the NASA/ESA Hubble Space Telescope obtained from the Space Telescope Science Institute, which is operated by the Association of Universities for Research in Astronomy, Inc., under NASA contract NAS 5-26555. These observations are associated with programs SNAP17070 and SNAP17506.

Observations reported here were obtained at the MMT Observatory, a joint facility of the University of Arizona and the Smithsonian Institution.

Some of the data presented herein were obtained at Keck Observatory, which is a private 501(c)3 nonprofit organization operated as a scientific partnership among the California Institute of Technology, the University of California, and the National Aeronautics and Space Administration. The Observatory was made possible by the generous financial support of the W. M. Keck Foundation.

The authors wish to recognize and acknowledge the very significant cultural role and reverence that the summit of Maunakea has always had within the Native Hawaiian community. We are most fortunate to have the opportunity to conduct observations from this mountain.

J.E.A. is supported by the international Gemini Observatory, a program of NSF NOIRLab, which is managed by the Association of Universities for Research in Astronomy (AURA) under a cooperative agreement with the U.S. National Science Foundation, on behalf of the Gemini partnership of Argentina, Brazil, Canada, Chile, the Republic of Korea, and the United States of America.

Time domain research by the University of Arizona team and D.J.S. is supported by National Science Foundation (NSF) grants 2108032, 2308181, 2407566, and 2432036 and the Heising-Simons Foundation under grant #2020-1864.

C.D.K. gratefully acknowledges support from the NSF through AST-2432037, the HST Guest Observer Program through HST-SNAP-17070 and HST-GO-17706, and from JWST Archival Research through JWST-AR-6241 and JWST-AR-5441.

W.J.-G. is supported by NASA through Hubble Fellowship grant HSTHF2-51558.001-A awarded by the Space Telescope Science Institute, which is operated for NASA by the Association of Universities for Research in Astronomy, Inc., under contract NAS 5-26555.

A.A.M., C.L., and N.R. are supported by DoE award No. DE-SC0025599. MMT Observatory access for A.M., C.L., and N.R. was supported by Northwestern University and the Center for Interdisciplinary Exploration and Research in Astrophysics (CIERA).

K.A.B. is supported by an LSST-DA Catalyst Fellowship; this publication was thus made possible through the support of grant 62192 from the John Templeton Foundation to LSST-DA.

Facilities: HST (ACS, WFC3), JWST (MIRI), Keck (LRIS), MAST (HLSP), MMT (Binospec, MMIRS).

Software: astropy (Astropy Collaboration et al. 2013, 2018, 2022), Dolphot (A. E. Dolphin 2000; A. Dolphin 2016), emcee (D. Foreman-Mackey et al. 2013), Light Curve Fitting (G. Hosseinzadeh & S. Gomez 2020; G. Hosseinzadeh et al. 2023a), LPipe (D. A. Perley 2019), MatPLOTLIB (J. D. Hunter 2007), NumPy (C. R. Harris et al. 2020), Photutils (L. Bradley et al. 2022), space_phot (J. Pierel 2024), SEP (E. Bertin & S. Arnouts 1996; K. Barbary 2016), WebbPSF (M. D. Perrin et al. 2012, 2014), WISeREP (O. Yaron & A. Gal-Yam 2012).

Appendix A Aperture versus PSF Photometry

In order to measure the flux in the MIRI images, we attempted several different photometric techniques, which we compared to the published Cycle 1 photometry in M. Shahbandeh et al. (2023). In this work, we report JWST MIRI PSF photometry of SN 2017eaw because this methodology resulted in values that are most consistent with previously published photometry. M. Shahbandeh et al. (2023) did PSF photometry on the stage 2 products, a method similar to the one we use for our photometry in Section 2.1. As shown in Figure 13 (purple diamonds and pink squares), the most significant offsets between our space_phot PSF photometry and the published photometry are at 18 and 21 μ m, both of which are filters where the photometric calibration maps were significantly updated²² between the publication of M. Shahbandeh et al. (2023) and the completion of this work, therefore this offset is unsurprising.

Aperture photometry methods were unable to reproduce the flux values measured by PSF photometry methods. Our initial photometry of SN 2017eaw was done using an aperture photometry method similar to that used in G. Hosseinzadeh et al. (2023b), on the Cycle 1 and 2 Level 3 I2D images of SN 2017eaw. The science and background apertures for a selection of the images for SN 2017eaw are shown in Figure 14. We choose the science aperture to enclose 60% of the light from the source based on the JWST/MIRI aperture correction (version 0014, in flight pedigree of 2022 May 25–2024 June 2). Background subtraction is done using the average of two circular regions on either side of the aperture. We find that in the case of SN 2017eaw, the diffraction spikes are minimal enough that using an annulus for background subtraction produces photometry which is consistent with that from the two circular aperture method. However, given the diffraction spikes and surroundings of the comparison stars in the field, we use two circular apertures for consistency. The locations of the two background regions were chosen to avoid diffraction spikes while remaining close to the science aperture. The background apertures are chosen to be on the same region of the sky for all exposures of the target. However, as shown in Figure 13 (green circles), this methodology results in fluxes that are systematically higher than those published in M. Shahbandeh et al. (2023).

Given the discrepancy between the aperture photometry and the M. Shahbandeh et al. (2023) values, in order to cross check our methodology we utilize a separate aperture photometry code originally designed to do photometry on NIRCAM highredshift galaxies described in R. Endsley et al. (2023), which was adapted to allow for aperture photometry on MIRI images. First, SEP (the Python library for Source Extraction and Photometry; E. Bertin & S. Arnouts 1996; K. Barbary 2016) is run on the F2100W image to choose an elliptical aperture which encloses >90% of the flux and we then use this aperture size for all filters. We chose F2100W since it is the reddest filter with a high signal-to-noise ratio point source at the location of SN 2017eaw, and therefore has the largest PSF. Second, SEP is run on all filters to mask out all objects in the field. This requires a background subtracted image. Given the complex background of the image, we opt to create 10"x10"

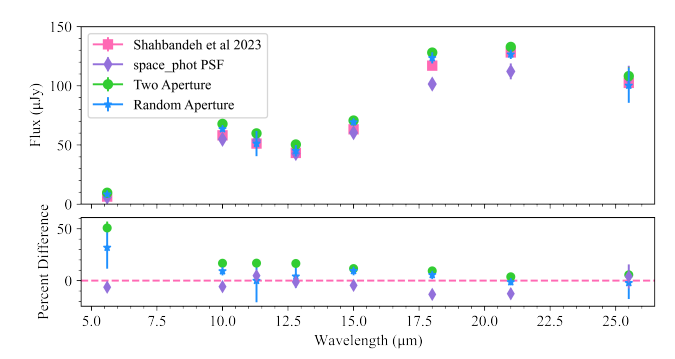


Figure 13. Comparison of aperture and PSF photometry methods for JWST/MIRI Cycle 1 observations of SN 2017eaw. Top: JWST/MIRI SED measured using the different photometric methods. The published values from M. Shahbandeh et al. (2023) are also plotted. The aperture methods result in fluxes that are higher than those reported for PSF methods. Bottom: Percent difference in flux from M. Shahbandeh et al. (2023) values for each photometry method in this work. The <code>space_phot</code> method is consistent with the M. Shahbandeh et al. (2023) values, therefore we report this photometry in Section 2.1. We note that significant changes were made to the MIRI PSFs (primarily >15 μ m) following in the publication of M. Shahbandeh et al. (2023), this is likely the cause of the discrepancy between the <code>space_phot</code> and the published values for the redder filters.

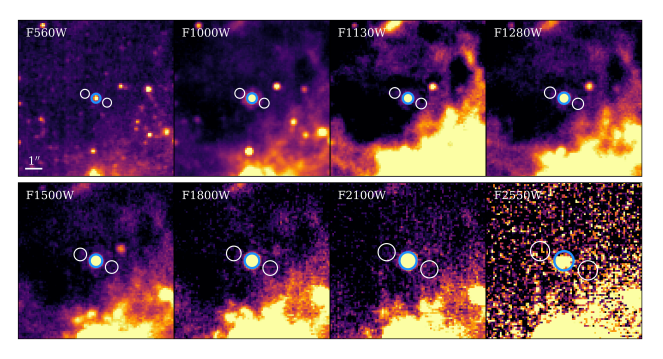


Figure 14. Aperture placement on Cycle 1 JWST/MIRI observations for the two aperture background photometry methods. The central blue circle is the science aperture. The two white circles on either side of the target are the apertures used for the background subtraction. We utilized the same aperture locations on the sky for the Cycle 2 observations. Background aperture locations were chosen to avoid diffraction spikes in both the Cycle 1 and Cycle 2 observations.

stamps centered around the SN position and measure the spatially varying background using SEP. This background is then subtracted from the image stamp. Third, we randomly place 50 apertures on the background subtracted image and measured their fluxes. The standard deviation in these measurements is the error in our photometry and the median value is subtracted off the final photometry to account for higher order background fluctuations. Finally, we apply an aperture correction determined by dropping the elliptical aperture used on the WebbPSF models (M. D. Perrin et al. 2012, 2014) for each filter and calculating the amount of total flux enclosed within the aperture.

As shown in Figure 13 (blue stars), the random aperture background method also yields flux values higher than those reported in M. Shahbandeh et al. (2023). However, because of how photometric errors are accounted for in the random aperture background method, the errors in these measurements are large. Therefore, the photometry from this method is roughly consistent with both the previously discussed aperture photometry method and M. Shahbandeh et al.'s (2023) PSF photometry.

²³ This work uses version 0056, details can be found at https://jwst-crds.stsci.edu/browse/jwst_miri_photom_0056.rmap.

Due to the discrepancy between the aperture and PSF photometry regardless of methodology, and the existence of published JWST/MIRI PSF photometry of SN 2017eaw, we opt to report only the PSF photometry discussed in Section 2.1 in this work. We note that M. Shahbandeh et al. (2023) subtract a background image, made by taking the sigmaclipped average of the individual dithers, from the level 2 images before doing PSF photometry. We opt to not do this since space phot fits the background alongside the PSF model and generally our photometry is consistent with M. Shahbandeh et al. (2023). Importantly, we do find that, regardless of the photometric method, the total mid-infrared flux of SN 2017eaw has decreased from Cycle 1 to Cycle 2. We caution that the aperture and PSF photometry of JWST/ MIRI data may not be consistent with each other and recommend using similar methods as reported in previous publications. This discrepancy may decrease over the course of the JWST mission as MIRI aperture corrections and PSF models continue to be updated.

Appendix B Dust Modeling Equations

In Section 3.4, we discuss the fitting methods for the optically thin, dusty sphere, and dusty shell models. Here, we present the luminosity equations used for all three of these dust models.

B.1. Optically Thin Model

For the optically thin case, we model the input luminosity as two components of dust, with temperatures $T_{\rm hot}$ and $T_{\rm cool}$ and masses $M_{\rm hot}$ and $M_{\rm cool}$. We note that in the optically thin case, $R_{\rm dust}$ is not well constrained. For each component, the input luminosity is set by:

$$L_{\nu,\text{dust}} = 4\pi \kappa_{\nu} M_{\text{dust}} B_{\nu} (T_{\text{dust}}), \tag{B1}$$

where $B_{\nu}(T)$ is the Planck function and κ_{ν} is the frequency-dependent opacity of the dust component. We calculate κ_{ν} from the absorption efficiency Q_{ν} , particle density $\rho_{\rm part}$, and particle size a:

$$\kappa_{\nu} = \frac{3Q_{\nu}}{4a\rho_{\text{part}}}.$$
 (B2)

In the optically thin case, the dust will not self-attenuate, so the total luminosity is just:

$$L_{\nu,\text{thin}} = 4\pi\kappa_{\nu}[M_{\text{hot}}B_{\nu}(T_{\text{hot}}) + M_{\text{cool}}B_{\nu}(T_{\text{cool}})], \tag{B3}$$

B.2. Dusty Sphere Model

In the dusty sphere case, we assume a sphere of dust with total mass $M_{\rm hot}+M_{\rm cool}$ and two temperature components ($T_{\rm hot}$ and $T_{\rm cool}$) inside a radius $R_{\rm outer}$ with an optical depth $\tau_{\nu}>0$. This model is geometrically similar to the dusty sphere model used in M. Shahbandeh et al. (2023). The luminosity of the dusty sphere is extinguished according to the escape probability from D. E. Osterbrock (1989, Appendix 2):

$$P_{\rm esc} = \frac{3}{4\tau_{\nu}} \left[1 - \frac{1}{2\tau_{\nu}^{2}} + \left(\frac{1}{\tau_{\nu}} + \frac{1}{2\tau_{\nu}^{2}} \right) e^{-2\tau_{\nu}} \right], \tag{B4}$$

here the frequency-dependent optical depth (τ_{ν}) to the center of a dust shell with bulk density ρ_{bulk} is:

$$\tau_{\nu} = \kappa_{\nu} \rho_{\text{bulk}} R_{\text{dust}} = \frac{3\kappa_{\nu} M_{\text{dust}}}{4\pi R_{\text{dust}}^2}.$$
 (B5)

For the dusty sphere model τ_{ν} is:

$$\tau_{\nu} = \frac{3\kappa_{\nu}(M_{\text{hot}} + M_{\text{cool}})}{4\pi R_{\text{outer}}^2}.$$
 (B6)

Thus, the full SED for the dusty sphere is modeled by:

$$L_{\nu,\text{sphere}} = \frac{4\pi^2 R_{\text{outer}}^2}{M_{\text{hot}} + M_{\text{cool}}} [M_{\text{hot}} B_{\nu}(T_{\text{hot}}) + M_{\text{cool}} B_{\nu}(T_{\text{cool}})] \times \left[1 - \frac{1}{2\tau_{\nu,\text{w}}^2} + \left(\frac{1}{\tau_{\nu,\text{w}}} + \frac{1}{2\tau_{\nu,\text{w}}^2}\right) e^{-2\tau_{\nu,\text{w}}}\right].$$
(B7)

B.3. Dusty Shell Model

We also fit a dusty shell model, with total dust mass $M_{\text{hot}} + M_{\text{cool}}$, inner radius R_{inner} , and outer radius R_{outer} , to the SED. For the dusty shell, the frequency-dependent optical depth (analogous to Equation (B5)) is:

$$\tau_{\nu} = \frac{3\kappa_{\nu}R_{\text{outer}}}{4\pi(R_{\text{outer}}^3 - R_{\text{inner}}^3)} (M_{\text{hot}} + M_{\text{cool}}).$$
 (B8)

The escape probability is similarly more complex because it must take the inner cavity, where $\tau_{\nu}=0$, into account. We use the escape probability expression worked out in E. Dwek & R. G. Arendt (2024):

$$P_{\rm esc} = \frac{1}{2\tau_{\nu}} \left[\frac{f(u, \tau_{\nu})}{f_0(u)} \right],$$
 (B9)

where

$$f(u, \tau_{\nu}) = \int_{0}^{x_{c}} [1 - e^{-2\tau_{\nu}x}] x \, dx$$

$$+ \int_{x_{c}}^{1} \left[1 - e^{-2\tau_{\nu}x} \left(1 - \sqrt{1 - \frac{1 - u^{2}}{x^{2}}} \right) \right] x \, dx, \quad (B10)$$

and

$$f_0(u) = \int_0^{x_c} x^2 dx + \int_{x_c}^1 \left[1 - \sqrt{1 - \frac{1 - u^2}{x^2}} \right] x^2 dx,$$
 (B11)

where $x_c = \sqrt{1 - u^2}$, $u = \frac{R_{\text{inner}}}{R_{\text{outer}}}$, and R_{inner} and R_{outer} are the inner and outer radii of the shell, respectively.

Which yields the total dusty shell luminosity:

$$L_{\nu,\text{shell}} = \frac{2\pi\kappa_{\nu}f(u, \tau_{\nu})}{\tau_{\nu}f_{0}(u)}$$

$$\times [M_{\text{hot}}B_{\nu}(T_{\text{hot}}) + M_{\text{cool}}B_{\nu}(T_{\text{cool}})]. \tag{B12}$$

Appendix C Cycle 2 Dust Models Excluding F770W and NIR Observations

No NIR or F770W data were taken coincident with the Cycle 1 observations of SN 2017eaw. The dust modeling presented here highlights the need for additional constraints of the hot component of the dust SED, especially for younger SNe like SN 2017eaw. Given the lack of constraints on the hot component at 1960 days, we also fit the 2330 days SED with the NIR and F770W photometry excluded so that the SEDs are directly comparable. These results are presented in the furthest right column of Table 3 and fits are displayed in Figure 15.

We find that the dust models without the NIR and F770W observations are consistent with the values determined for Cycle 1. The Cycle 2 models that exclude NIR and F770W photometry tend to favor lower temperatures for the hot components than those found for Cycle 1. Given that the hotter dust component is set by only F560W in these fits, we attribute the decrease in temperature to the decrease in F560W flux. Without NIR observations, it is impossible to track the temperature evolution of the hot dust component. This uncertainty highlights the need for NIR observations to complement further SNe dust studies. In the case of SN 2017eaw, the majority of the dust mass is in the cool component and the MIRI observations alone are sufficient to suggest that the dust mass of SN 2017eaw did not markedly increase over the course of a year. However, we caution that this may not be the situation for every SNe, therefore NIR observations are crucial to understanding the dust budget of CCSNe.

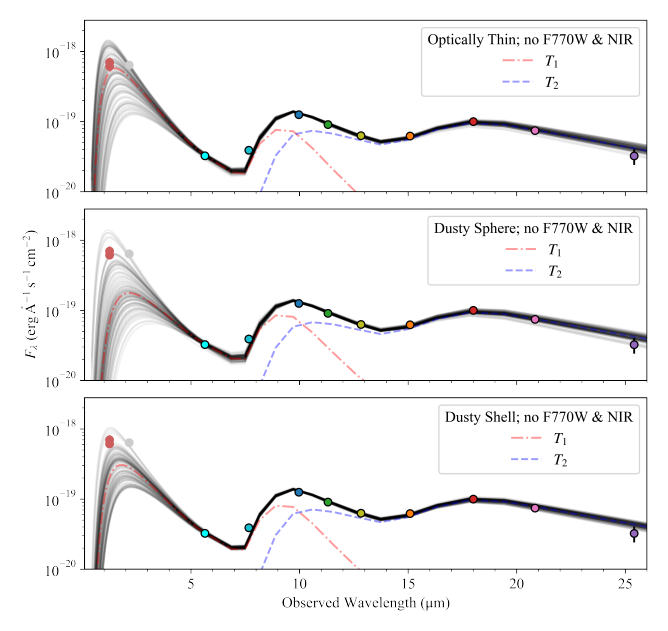


Figure 15. The best-fitting double silicate dust models for the Cycle 2 SEDs when F770W and the NIR bands are excluded. The NIR and F770W fluxes are plotted for comparison. The NIR data in particular are vital to constraining the hot dust component. The observed NIR fluxes are at the high end of the range of fits for the dusty sphere and shell models which assume $\tau_{\nu} > 0$.

ORCID iDs

```
Jennifer E. Andrews https://orcid.org/0000-0003-0123-0062
Emma R. Beasor https://orcid.org/0000-0003-4666-4606
K. Azalee Bostroem https://orcid.org/0000-0002-4924-444X
Yize Dong (董一泽) fi https://orcid.org/0000-0002-7937-6371
Emily Hoang https://orcid.org/0000-0003-2744-4755
Griffin Hosseinzadeh https://orcid.org/0000-0002-0832-2974
Brian Hsu https://orcid.org/0000-0002-9454-1742
Wynn Jacobson-Galán https://orcid.org/0000-0003-
1103-3409
Daryl Janzen https://orcid.org/0000-0003-0549-3281
Jacob Jencson  https://orcid.org/0000-0001-5754-4007
Saurabh W. Jha https://orcid.org/0000-0001-8738-6011
Charles D. Kilpatrick https://orcid.org/0000-0002-
5740-7747
Lindsey A. Kwok https://orcid.org/0000-0003-3108-1328
Chang Liu https://orcid.org/0000-0002-7866-4531
M. J. Lundquist https://orcid.org/0000-0001-9589-3793
Darshana Mehta https://orcid.org/0009-0008-9693-4348
Adam A. Miller https://orcid.org/0000-0001-9515-478X
Aravind P. Ravi https://orcid.org/0000-0002-7352-7845
Nabeel Rehemtulla https://orcid.org/0000-0002-5683-2389
Nicolás Meza Retamal https://orcid.org/0000-0002-
7015-3446
Manisha Shrestha https://orcid.org/0000-0002-4022-1874
Nathan Smith https://orcid.org/0000-0001-5510-2424
Stefano Valenti https://orcid.org/0000-0001-8818-0795
Lily Whitler https://orcid.org/0000-0003-1432-7744
```

References

```
Andrews, J. E., Gallagher, J. S., Clayton, G. C., et al. 2010, ApJ, 715, 541
Arendt, R. G., Boyer, M. L., Dwek, E., et al. 2023, ApJ, 959, 95
Arendt, R. G., Dwek, E., Bouchet, P., et al. 2016, AJ, 151, 62
Arendt, R. G., Dwek, E., Bouchet, P., et al. 2020, ApJ, 890, 2
Astropy Collaboration, Price-Whelan, A. M., Lim, P. L., et al. 2022, ApJ,
  935, 167
Astropy Collaboration, Price-Whelan, A. M., Sipőcz, B. M., et al. 2018, AJ,
Astropy Collaboration, Robitaille, T. P., Tollerud, E. J., et al. 2013, A&A,
  558, A33
Barbary, K. 2016, JOSS, 1, 58
Bertin, E., & Arnouts, S. 1996, A&AS, 117, 393
Bevan, A., & Barlow, M. J. 2016, MNRAS, 456, 1269
Bevan, A., Barlow, M. J., & Milisavljevic, D. 2017, MNRAS, 465, 4044
Bianchi, S., & Schneider, R. 2007, MNRAS, 378, 973
Bode, M. F., & Evans, A. 1980, MNRAS, 193, 21P
Bostroem, K. A., Zapartas, E., Koplitz, B., et al. 2023, AJ, 166, 255
Bouchet, P., Dwek, E., Danziger, J., et al. 2006, ApJ, 650, 212
Bouchet, P., García-Marín, M., Lagage, P. O., et al. 2015, PASP, 127, 612
Bouchet, P., Gastaud, R., Coulais, A., et al. 2024, ApJ, 965, 51
Bradley, L., Sipőcz, B., Robitaille, T., et al. 2022, astropy/photutils: v1.6.0,
  Zenodo, doi:10.5281/zenodo.7419741
Bushouse, H., Eisenhamer, J., Dencheva, N., et al. 2025, JWST Calibration
  Pipeline, v1.18.0, Zenodo, doi:10.5281/zenodo.15178003
Buta, R. J., & Keel, W. C. 2019, MNRAS, 487, 832
Chambers, K. C., Magnier, E. A., Metcalfe, N., et al. 2016, arXiv:1612.05560
Chastenet, J., De Looze, I., Hensley, B. S., et al. 2022, MNRAS, 516, 4229
Cigan, P., Matsuura, M., Gomez, H. L., et al. 2019, ApJ, 886, 51
Clayton, G. C., Wesson, R., Fox, O. D., et al. 2025, ApJ, 991, 133
Colangeli, L., Mennella, V., Palumbo, P., Rotundi, A., & Bussoletti, E. 1995,
   A&AS, 113, 561
Dalcanton, J. J., Williams, B. F., Lang, D., et al. 2012, ApJS, 200, 18
De Looze, I., Barlow, M. J., Swinyard, B. M., et al. 2017, MNRAS, 465, 3309
Dessart, L. 2024, arXiv:2405.04259
Dessart, L., Gutiérrez, C. P., Kuncarayakti, H., Fox, O. D., & Filippenko, A. V.
   2023, A&A, 675, A33
Dessart, L., & Hillier, D. J. 2022, A&A, 660, L9
Dessart, L., Hillier, D. J., & Sarangi, A. 2025, A&A, 698, A293
Dolphin, A., 2016 DOLPHOT: Stellar Photometry, Astrophysics Source Code
  Library, ascl:1608.013
```

Dolphin, A. E. 2000, PASP, 112, 1383

```
Draine, B. T. 1985, ApJS, 57, 587
Draine, B. T., & Li, A. 2007, ApJ, 657, 810
Dunne, L., Eales, S., Ivison, R., Morgan, H., & Edmunds, M. 2003, Natur,
  424, 285
Dwek, E. 1983, ApJ, 274, 175
Dwek, E., & Arendt, R. G. 2024, RNAAS, 8, 194
Dwek, E., Arendt, R. G., Bouchet, P., et al. 2010, ApJ, 722, 425
Endsley, R., Stark, D. P., Whitler, L., et al. 2023, MNRAS, 524, 2312
Fabbri, J., Otsuka, M., Barlow, M. J., et al. 2011, MNRAS, 418, 1285
Fabricant, D., Fata, R., Epps, H., et al. 2019, PASP, 131, 075004
Fassia, A., Meikle, W. P. S., & Spyromilio, J. 2002, MNRAS, 332, 296
Foreman-Mackey, D., Hogg, D. W., Lang, D., & Goodman, J. 2013, PASP,
Fox, O. D., Chevalier, R. A., Dwek, E., et al. 2010, ApJ, 725, 1768
Fox, O. D., Chevalier, R. A., Skrutskie, M. F., et al. 2011, ApJ, 741, 7
Fox, O. D., Szalai, T., Andrews, J., et al. 2021, Are Supernovae Dust
   Factories?, JWST Proposal. Cycle 1 ID #2666, STSci https://www.stsci.
   edu/jwst-program-info/download/jwst/pdf/2666/
Gall, C., Hjorth, J., & Andersen, A. C. 2011, A&ARv, 19, 43
Gallagher, J. S., Sugerman, B. E. K., Clayton, G. C., et al. 2012, ApJ, 753, 109
Gomez, S., Temim, T., Fox, O., et al. 2024, arXiv:2408.15397
Harris, C. R., Millman, K. J., van der Walt, S. J., et al. 2020, Natur, 585, 357
Hashimoto, T., Inoue, A. K., Mawatari, K., et al. 2019, PASJ, 71, 71
Hosseinzadeh, G., Bostroem, K. A., & Gomez, S. 2023a, Light Curve Fitting,
   v0.8.0, Zenodo, doi:10.5281/zenodo.7872772
Hosseinzadeh, G., & Gomez, S. 2020, Light Curve Fitting, v0.2.0, Zenodo,
   doi:10.5281/zenodo.4312178
Hosseinzadeh, G., Sand, D. J., Jencson, J. E., et al. 2023b, ApJL, 942, L18
Hunter, J. D. 2007, CSE, 9, 90
Indebetouw, R., Matsuura, M., Dwek, E., et al. 2014, ApJL, 782, L2
Jones, O. C., Kavanagh, P. J., Barlow, M. J., et al. 2023, ApJ, 958, 95
Kilpatrick, C. D., & Foley, R. J. 2018, MNRAS, 481, 2536
Kotak, R., Meikle, W. P. S., Farrah, D., et al. 2009, ApJ, 704, 306
Laor, A., & Draine, B. T. 1993, ApJ, 402, 441
Lodders, K., & Fegley, B. 1997, in AIP Conf. Ser. 402, Astrophysical
   Implications of the Laboratory Study of Presolar Materials, ed.
   T. J. Bernatowicz & E. Zinner (San Francisco, CA: AIP), 391
Lucy, L. B., Danziger, I. J., Gouiffes, C., & Bouchet, P. 1989, in IAU Colloq.
   120: Structure and Dynamics of the Interstellar Medium, 350, ed.
   G. Tenorio-Tagle, M. Moles, & J. Melnick (Berlin: Springer), 164
Maguire, K., Jerkstrand, A., Smartt, S. J., et al. 2012, MNRAS, 420, 3451
Maiolino, R., Schneider, R., Oliva, E., et al. 2004, Natur, 431, 533
Markov, V., Gallerani, S., Ferrara, A., et al. 2024, NatAs, 9, 458
Marrone, D. P., Spilker, J. S., Hayward, C. C., et al. 2018, Natur, 553, 51
Matsuura, M., Boyer, M., Arendt, R. G., et al. 2024, MNRAS, 532, 3625
Matsuura, M., Dwek, E., Barlow, M. J., et al. 2015, ApJ, 800, 50
Matsuura, M., Dwek, E., Meixner, M., et al. 2011, Sci, 333, 1258
Mattila, S., Meikle, W. P. S., Lundqvist, P., et al. 2008, MNRAS, 389, 141
McLeod, B., Fabricant, D., Nystrom, G., et al. 2012, PASP, 124, 1318
Morgan, H. L., Dunne, L., Eales, S. A., Ivison, R. J., & Edmunds, M. G. 2003,
    ApJL, 597, L33
Morgan, H. L., & Edmunds, M. G. 2003, MNRAS, 343, 427
Nanni, A., et al. 2025, ApJL, 988, L5
Niculescu-Duvaz, M., Barlow, M. J., Bevan, A., et al. 2022, MNRAS,
   515, 4302
Niculescu-Duvaz, M., Barlow, M. J., Dunn, W., et al. 2023, MNRAS,
  519, 2940
Nozawa, T., Kozasa, T., Habe, A., et al. 2007, ApJ, 666, 955
Oke, J. B., Cohen, J. G., Carr, M., et al. 1995, PASP, 107, 375
Osterbrock, D. E. 1989, Astrophysics of Gaseous Nebulae and Active Galactic
   Nuclei (Mill Valley, CA: Univ. Science Books)
```

```
Perley, D. A. 2019, PASP, 131, 084503
Perrin, M. D., Sivaramakrishnan, A., Lajoie, C.-P., et al. 2014, Proc. SPIE,
  9143, 91433X
Perrin, M. D., Soummer, R., Elliott, E. M., Lallo, M. D., &
  Sivaramakrishnan, A. 2012, Proc. SPIE, 8442, 84423D
Pierel, J. 2024, Space-Phot: Simple Python-Based Photometry for Space
  Telescopes, v1, Zenodo, doi:10.5281/zenodo.12100100
Pierel, J. D. R., Frye, B. L., Pascale, M., et al. 2024, ApJ, 967, 50
Pozzo, M., Meikle, W. P. S., Fassia, A., et al. 2004, MNRAS, 352, 457
Priestley, F. D., Arias, M., Barlow, M. J., & De Looze, I. 2022, MNRAS,
  509, 3163
Rho, J., Geballe, T. R., Banerjee, D. P. K., et al. 2018, ApJL, 864, L20
Rho, J., Kozasa, T., Reach, W. T., et al. 2008, ApJ, 673, 271
Rieke, G. H., Wright, G. S., Böker, T., et al. 2015, PASP, 127, 584
Rizzo Smith, M., Kochanek, C. S., & Neustadt, J. M. M. 2023, MNRAS,
  523, 1474
Rui, L., Wang, X., Mo, J., et al. 2019, MNRAS, 485, 1990
Sand, D. J., Andrews, J., Beasor, E., et al. 2023, Is There Enough? Cosmic
  Dust Formation in Normal Core-collapse Supernovae in the First 5 Years
  Post-explosion, JWST Proposal. Cycle 2 ID #3295, STSci https://www.
  stsci.edu/jwst/phase2-public/3295.pdf
Sarangi, A. 2022, A&A, 668, A57
Sarangi, A., Matsuura, M., & Micelotta, E. R. 2018, SSRv, 214, 63
Sarangi, A., Zsiros, S., Szalai, T., et al. 2025, arXiv:2504.20574
Schneider, R., & Maiolino, R. 2024, A&ARv, 32, 2
Shahbandeh, M., Ashall, C., Hoeflich, P., et al. 2024, arXiv:2401.14474
Shahbandeh, M., Fox, O. D., Temim, T., et al. 2025, ApJ, 985, 262
Shahbandeh, M., Sarangi, A., Temim, T., et al. 2023, MNRAS, 523,
Silvia, D. W., Smith, B. D., & Shull, J. M. 2010, ApJ, 715, 1575
Skrutskie, M. F., Cutri, R. M., Stiening, R., et al. 2006, AJ, 131, 1163
Smith, N., Foley, R. J., & Filippenko, A. V. 2008, ApJ, 680, 568
Smith, N., Silverman, J. M., Chornock, R., et al. 2009, ApJ, 695, 1334
Sugerman, B. E. K. 2003, AJ, 126, 1939
Szalai, T., & Vinkó, J. 2013, A&A, 549, A79
Szalai, T., Vinkó, J., Balog, Z., et al. 2011, A&A, 527, A61
Szalai, T., Vinkó, J., Könyves-Tóth, R., et al. 2019a, ApJ, 876, 19
Szalai, T., Zsíros, S., Fox, O. D., Pejcha, O., & Müller, T. 2019b, ApJS,
  241.38
Szalai, T., Zsíros, S., Jencson, J., et al. 2025, A&A, 697, A132
Tinyanont, S., Fox, O. D., Shahbandeh, M., et al. 2025, ApJ, 985, 198
Tinyanont, S., Kasliwal, M. M., Fox, O. D., et al. 2016, ApJ, 833, 231
Tinyanont, S., Kasliwal, M. M., Krafton, K., et al. 2019, ApJ, 873, 127
Todini, P., & Ferrara, A. 2001, MNRAS, 325, 726
Truelove, J. K., & McKee, C. F. 1999, ApJS, 120, 299
Tsvetkov, D. Y., Shugarov, S. Y., Volkov, I. M., et al. 2018, AstL, 44,
Van Dyk, S. D., de Graw, A., Baer-Way, R., et al. 2023, MNRAS, 519,
  471
Van Dyk, S. D., Zheng, W., Maund, J. R., et al. 2019, ApJ, 875, 136
Weil, K. E., Fesen, R. A., Patnaude, D. J., & Milisavljevic, D. 2020, ApJ,
Wesson, R., Barlow, M. J., Matsuura, M., & Ercolano, B. 2015, MNRAS,
  446, 2089
Williams, B. F., Lang, D., Dalcanton, J. J., et al. 2014, ApJS, 215, 9
Witstok, J., Shivaei, I., Smit, R., et al. 2023, Natur, 621, 267
Wright, G. S., Rieke, G. H., Glasse, A., et al. 2023, PASP, 135, 048003
Yaron, O., & Gal-Yam, A. 2012, PASP, 124, 668
Zsíros, S., Nagy, A. P., & Szalai, T. 2022, MNRAS, 509, 3235
Zsíros, S., Szalai, T., De Looze, I., et al. 2024, MNRAS, 529, 155
```